

DISS. ETH NO. 21458

**CHEMICAL VAPOR DEPOSITION OF  
GRAPHENE ON COPPER**

A dissertation submitted to

ETH ZURICH

for the degree of

DOCTOR OF SCIENCE

presented by

KEMAL CELEBI

M. Sc. Physics,

Massachusetts Institute of Technology

Born on February 13th 1982, citizen of Turkey

accepted on the recommendation of

Prof. Dr. Hyung Gyu Park, examiner

Prof. Dr. Dimos Poulikakos, co-examiner

Zurich, 2013



## **Acknowledgments**

This thesis has been completed at ETH Zurich with the support of many contributors, to whom I would like to express my sincere thankfulness.

I would like to express my heartfelt gratitude to Professor Park, for his supervision, financial support on this project, patience and admirable will in hard work.

My sincere thanks go to Dr. Ken Teo for his very valuable collaboration and suggestions in so many aspects of this work. I also very much appreciate Matt's contributions in our fruitful collaboration.

I would like to thank Professor Robertson for his enlightening suggestions in our collaboration, and for his evaluation of this project. I also owe gratitude to Professor Poulidakos, for accepting to evaluate my thesis.

Many thanks to the experienced staff and members of FIRST and BRNC cleanrooms, and EMEZ microscopy center, for their valuable teaching and suggestions on microfabrication and characterization. I would like to particularly mention Otte Homan, Sandro Bellini, Roland Germann, David Webb, Ronald Grundbacher and Karsten Kunze.

My heartfelt thanks and appreciation to my fellow group mates: Seul Ki, Ali, Dr. Choi, Jakob, Nuri, Amir, Ning and Meng Meng; for sharing the ups and downs throughout this journey. Special thanks to Seul Ki for motivating me throughout the difficult times.

I also would like to appreciate the highly valuable contribution of my master's students: Roman, PJ, Georgios and Patrick.

Without the persistence of my parents and my wife, probably this page would not exist. I love you all.



## Abstract

The era of two-dimensional materials has begun with graphene. It is the first artificially-isolated single-atom-thick material, which is also an exceptional example of its kind. With its extraordinary physical and chemical properties, it has become hugely popular among scientists and technologists in a timeframe of less than a decade.

When first isolated, graphene was a subject of the fundamental research by condensed matter physicists. Later, the hopes on graphene's applicability have leapt forward by its synthesis on sacrificial substrates by chemical vapor deposition (CVD). Thus, a great deal of interest in research and development of graphene has risen all over the world.

The present thesis addresses the synthesis of graphene by CVD on copper, which has become the most popular catalyst for graphene growth. The entire CVD process, as well as the sacrificial transfer methods is studied in this project.

One of the first demonstrations of ethylene-based graphene growth is presented herein. The methods for substrate selection and preparation, graphene growth and transfer to rigid and porous substrates are explained in detail. Low defect density ( $I_{G'}/I_G = 1.82 \pm 0.25$ ) and high monolayer covering (98.4%) have been achieved, yielding a charge mobility of  $3,600 \text{ cm}^2 \text{ V}^{-1} \text{ s}^{-1}$ .

A significant study on the graphene growth kinetics and mechanisms is also reported in the present thesis. It has been previously claimed that graphene growth on copper by CVD is dominated solely by crystallization from the surface initially supersaturated with carbon adatoms, which implies that the growth is independent of hydrocarbon addition after the nucleation phase. Here, an alternative growth model is presented, based on the observations that oppose this claim. A Gompertzian sigmoidal growth kinetics model described here supports the postulate that the graphene CVD can be controlled by adsorption-desorption dynamics and the dispersive kinetic processes of catalytic dissociation and dehydrogenation of carbon precursors on copper.

A quantitative analysis of the graphene crystal morphology presented in this thesis claims that the sublimation of copper catalyst is critically important in defining the crystal shapes. A suppression of this sublimation can result in improved hexagonal morphology, which could provide better grain connectivity.

Finally, an improved graphene transfer method is described. The differences in the initial and recent transfer processes are explained. Substantial advancements in the cleanliness and the mechanical stability of transferred graphene are shown to yield high quality freestanding graphene on large-scale pore arrays.

## Zusammenfassung

Mit der Entdeckung von Graphene hat die Ära der zweidimensionalen Materialien begonnen. Graphene ist das erste künstlich isolierte Material, das aus nur einer Lage von Atomen besteht. Mit seinen außergewöhnlichen physikalischen und chemischen Eigenschaften erfreut sich es grosser Beliebtheit unter Wissenschaftlern und Technologen.

Während kurz nach der Entdeckung, Graphene vor Allem Gegenstand der Grundlagenforschung in der Festkörperphysik war, wurden schnell verschiedene Anwendungsgebiete für Graphene entdeckt. Insbesondere die Synthese von Graphene auf Opfersubstraten durch chemische Gasphasenabscheidung (CVD) ermöglicht die Nutzung von Graphene in verschiedensten Anwendungen. Weltweit wurden daher große Mengen an Forschungsgeldern in die Erforschung von Graphene investiert.

Die vorliegende Arbeit befasst sich mit der CVD-Synthese von Graphene auf Kupfer, dem meist benutzten Katalysator für Graphene-Wachstum. Das gesamte CVD-Syntheseverfahren, sowie die Opferschicht Transferverfahren werden in diesem Projekt untersucht.

Einer der ersten Nachweise des Ethylene basierenden Graphene-Wachstums wird erbracht. Ausserdem werden Methoden der Substratauswahl und -vorbereitung, sowie die Graphene Synthese und der Transfer zum starren und porösen Substrate im Detail erläutert. Das synthetisierte Graphene weist eine niedrige Defektdichte ( $I_G/I_G = 1.82 \pm 0.25$ ) auf, besteht aus 98.4% Monolage und hat eine Ladungsträgerbeweglichkeit von  $3600 \text{ cm}^2 \text{ V}^{-1} \text{ s}^{-1}$ .

Eine massgebliche Untersuchung der Kinetik und der Mechanismen des Graphene-Wachstums wird präsentiert. Bisher ging die Forschung davon aus, dass das die CVD Synthese von Graphene auf Kupfer durch die Kristallisation von Kohlenstoff auf der Oberfläche, die zuvor durch Kohlenstoff Adatome übersättigt wurde, dominiert wird. Dies wiederum bedeutet, dass das Wachstum unabhängig von Kohlenwasserstoff-Zugabe nach der Nukleationsphase ist.

Detaillierte Beobachtungen der Wachstumskinetik unterstützen ein alternatives Wachstumsmodell. Das Gompertz-Funktion-Wachstumskinetikmodell, das hier beschrieben wird, unterstützt das Postulat, dass die Graphenesynthese durch Adsorptions-Desorptions-Dynamik und dispersive, kinetische Prozesse, der katalytischen Dissoziation und der Wasserstoffabspaltung des Kohlenstoff-Precursors auf Kupfer, kontrolliert werden kann.

Eine quantitative Analyse der Graphen-Flocken-Morphologie in dieser Arbeit zeigt, dass die Stärke der Sublimation des Kupfer-Katalysators die Form der Graphene Flocke definiert. Wird die Sublimation unterdrückt, entsteht eine hexagonale Morphologie und die Korngrenzen Verbindung kann verbessert werden.

Schließlich wird ein verbessertes Graphene-Transferverfahren beschrieben und die Unterschiede zu bisherigen Transferprozessen aufgezeigt. Erhebliche Fortschritte bei der Sauberkeit und der mechanischen Stabilität des übertragenen Graphenes, ermöglichen die Herstellung von hoch qualitativen, frei stehenden Graphenmembranen auf großen Loch-Arrays.



## Table of Contents

Acknowledgments.....	i
Abstract .....	iii
Zusammenfassung .....	v
1 Introduction .....	11
Thesis Outline .....	16
Nomenclature .....	18
2 Preparation for Growth: Substrate Effects on Graphene Quality	20
2.1 Abstract .....	20
2.2 Introduction and Literature Review .....	21
2.3 Influence of Copper Foil Composition .....	23
Foil Contaminants .....	23
Surface Coatings from the Foil Production .....	24
2.4 Annealing and Surface Crystallinity .....	26
2.5 Additional Thin Metal Layers on Copper Foils.....	27
2.6 Conclusions .....	29
3 Growth Conditions and Characterization of the Graphene .....	31
3.1 Abstract .....	31
3.2 Introduction .....	32
3.3 Materials and Methods.....	33
Growth conditions .....	33
Characterization Methods .....	34
3.4 Results and Discussion .....	36
Raman Spectroscopy on Copper .....	36
Characterization of Graphene Crystals .....	38
Characterization of the Continuous Graphene.....	44
3.5 Conclusions .....	46

4 CVD Kinetics and Fundamental Mechanisms that Govern the Growth.....	48
4.1 Abstract .....	48
4.2 Introduction .....	49
Nucleation of Graphene on Copper .....	49
Graphene Growth Kinetics.....	51
Reaction Energetics.....	52
4.3 Experimental Methods .....	56
4.4 Growth Kinetics .....	59
4.5 Thermal Behavior and Fundamental Mechanisms .....	65
4.6 Conclusions .....	71
5 Crystal Morphology and Growth of Additional Layers .....	74
5.1 Abstract .....	74
5.2 Introduction.....	75
Crystal Morphology .....	75
Secondary Layers.....	77
5.3 Results and Discussion .....	79
Quality and Defects .....	83
5.5 Conclusions .....	85
6 Graphene Transfer .....	87
6.1 Abstract .....	87
6.2 Introduction.....	88
Transfer Methods .....	88
Cleanliness .....	89
6.3 Materials and Methods.....	91
Early Method .....	91
Improved Method.....	91
6.4 Results and Discussion .....	93

Cleanliness .....	93
Transfer Yield onto Micromeshes.....	94
6.5 Conclusions .....	97
7 Epilogue .....	99
7.1 Conclusions .....	99
7.2 Outlook.....	101
Scaling-up Schemes.....	101
Direct Synthesis on Insulating Substrates.....	102
Fundamental Studies .....	103
Bibliography.....	105
Curriculum Vitae .....	119
List of Publications .....	120



## 1 Introduction

Parts of this chapter have been submitted for publication in *CRC Handbook of Graphene Science*.

Last two decades have seen a phenomenal shift of the dimensionality paradigm in materials processing. First, the one-dimensional carbon nanotube (CNT) has arisen, pushing the envelope of nanotechnology with it but coming short of processability. Then graphene has arrived, bringing the complexity and processability at two dimensions alongside. It is the simultaneous existence of complex structures with reasonable ease of processing that makes this two-dimensional material so attractive to technologists. This dimensionality is actually what has rendered Si-based electronics popular in our everyday life. Given this fact, it may be no exaggeration to state that the new era of two-dimensional materials has begun, with graphene rising up as the first of its kind.

Since its first isolation [1], graphene has been widely studied and shown to possess a wide range of unique properties such as extremely large charge mobilities up to  $200,000 \text{ cm}^2\text{V}^{-1}\text{s}^{-1}$  [2-4], linear dispersion resulting in massless Dirac fermions [5-7], a near zero bandgap resulting in saturable optical absorption [8], tunable bandgap [9], unprecedented mechanical strength (1 TPa tensile modulus) [10] and one of the highest thermal conductivities ever reported ( $5,300 \text{ Wm}^{-1}\text{K}^{-1}$ ), second only to superfluid helium [11].

Most studies investigating the fundamental properties of graphene have been performed using mechanically exfoliated graphene from highly oriented pyrolytic graphite (HOPG) or kish sources [1]. The high graphitic quality and cleanliness of this method have rendered this crystallographically ideal material perfectly suited as a test-bed for fundamental exploration. Indeed, this is how many, if not all, of the above properties were measured in practice. However, exfoliation techniques can only provide micrometer- and sub-micrometer-sized graphene crystal at random and uncontrolled locations, and despite a wide variety of chemical and mechanical exfoliation techniques

available and compatible with an arbitrary range of substrates, such approaches are unsuitable for technological purposes due to issues with scaling and reproducibility.

Given the unquestionably huge catalogue of exciting mechanical, optical and electronic properties demonstrated by graphene it is evidently a very promising material for technological applications such as flexible transparent conductors [12, 13], integrated circuit elements [14], high-frequency (GHz) transistors [15-17], ultracapacitors [18], battery electrodes [19, 20], desalination membranes [21], passivation layers [22, 23] and composite materials [24], to list but a few. All of these applications require large area graphene produced *via* scalable means. Thus, alternative isolation methods to mechanical cleavage are of critical interest, with particular interest on direct chemical synthesis. One example of this alternative approach is to use other top-down methods based on chemical exfoliation [25] which employ agitated intercalated graphite or chemically reduced graphene oxide in order to produce large quantities of crystal that can, when couple to various mechanical deposition techniques - such as casting, spray casting, Meyer rod, Langmuir Blodgett, screen printing, and electrophoretic deposition - coat extremely large surfaces [12, 26]. However, the resulting layer is an ensemble of graphitic material that is far from having the high quality, and subsequent properties therein, of the graphene monolayer due to the out-of-plane inter-crystal connectivity, tunnel barrier dominance, and altered chemical structure. As such, atomistic, or bottom-up, synthesis methods are the sole option to obtain high quality continuous monolayer of graphene.

Early work on graphene synthesis focused on epitaxy on silicon carbide (SiC) by removal of the Si atoms from the crystalline surface became popular among researchers due to its high quality [27-29]. This method has proven potential and has been used to demonstrate some of the fastest GHz circuits ever produced [30]. Unfortunately, the silicon carbide substrate is particularly expensive, confining the commercial feasibility to very high, aviation performance electronics. Moreover, such silicon sublimation processes require extremely high temperatures (*ca.* 1500 °C) making it incompatible with many substrates as well as increasing the per-unit-area cost of the synthesized material even more. Direct chemical assembly of benzene

sub-units has also been investigated [31], and though the feasibility of the approach has been evidenced, the material is as yet limited in terms of areal coverage and graphitic quality. Perhaps the most industrially viable approach is chemical vapor deposition (CVD). CVD of graphene is emerging as the preferred method of synthesizing graphene for almost all applications, attributed in part to wide process control, large-area compatibility, and technique familiarity of the CMOS foundries.

The history of graphene growth on metals can be tracked to more than half a century ago, with the first reports of monolayer and few layer graphite on Pt [32] and Ni [33]. At the time the interpretation of the observed monolayers to be of a graphitic nature was not always immediate [34]. The lack of interest in graphene has limited further research for a few decades. It was not until 2004 when the mechanical exfoliation method by Novoselov *et al.* [1] nourished the exploration on graphene and its production, much to the surprise of fervent Mermin followers who have believed the isolation of monolayer materials at finite temperatures was unphysical due to inherent thermodynamic instabilities of their lattices [35-37]. Thus, traditional methods based on direct growth were revived. Initial works in this period started with nickel-based growths [38] and continued by demonstrations on other metals. So far, graphene has been synthesized on polycrystalline Ni [39, 40], Fe [41], Au [42], stainless steel [43], and single crystals of Ru (0001) [44, 45], Ir (111) [46, 47], Rh (111) [48], Pt (111) [49, 50], and Pd (111) [51]. Since these metals can dissolve a large amount of carbon in bulk, the growth mechanism is mainly precipitation-based, with additional contributions from decomposition of the precursors on the metal surface. During cool-down the carbon from the bulk precipitates on the surface and forms the graphitic layers. Nevertheless, many of these catalysts including materials processing cost are quite expensive, as most of them are single crystalline metals of extremely high purity. Furthermore, controlling the number of layers during the growth is also proved challenging. Nevertheless, conventional metallurgical approaches were adopted to achieve monolayer growth including rapid quenching and more exotic means of direct engineering of the catalyst, such as developing binary alloys [52-54]. Meanwhile, lattice mismatch between graphene and the catalyst metals (with the exception of nickel, with a mismatch of less than 1%)

became an important hurdle. Lattice mismatch stimulates corrugation and wrinkle formation altering the intrinsic properties of graphene, such as the strain dependent work function, and producing Moire patterns [55, 56], often undesired for most purposes. Substrate interactions in particular with Ru (0001) can also cause modifications in the electronic band structure [45]. So far, only polycrystalline nickel has been demonstrated to yield reasonable quality graphene (*i.e.*, a charge mobility of  $3,700 \text{ cm}^2\text{V}^{-1}\text{s}^{-1}$ ) at low cost, scalable size, and low lattice mismatch [39]. However, even nickel has been surpassed by the controlled growths enabled by copper. At present, copper-based CVD is by far the most popular production method for large-scale graphene [57]. State of the art copper-based CVD graphene is now extremely graphitic and approaching a point where it can yield almost as good electronic quality of individual mechanically exfoliated crystal [58, 59], while scaling to hundreds of meters squared by emerging roll-to-roll processes [60].

This thesis focuses on the graphene synthesis by CVD on copper. All the process steps starting from the substrate preparation to the transfer of the end product are presented in detail. In particular, the kinetics of the CVD process and the fundamental mechanisms that govern the growth are systematically studied. Crystal morphology and secondary nucleations are also discussed.

The beginning of this project coincided with the first report of copper-based CVD of graphene. During the journey for the preparation of this thesis the relevant research field has gone through its embryonic stage. The early CVD recipes have been published, initial studies on the understanding of the fundamentals of the CVD process has been reported, and today's most common processes have been developed for better and cleaner handling of graphene, with particularly great improvements in the transfer methods.

The contribution of this project during this early stage of the field is twofold. First, one of the earliest ethylene-based CVD syntheses of graphene on copper has been reported. Second, one of the few important studies on the growth kinetics has been published. With this study, the fundamental mechanism that governs the kinetics of the CVD growth of graphene has been found to be the catalytic dissociative dehydration of ethylene on copper surface. Along with



the reported sigmoidal growth curves that support the role of the continual carbon supply, this finding has become the first systematic evidence against a purely supersaturation-driven growth [61].

## Thesis Outline

This thesis consists of seven chapters, including the introductory and the concluding chapters. This project is mainly experimental work, which is presented in Chapter 2 through Chapter 6. Each chapter has a summarizing abstract and a conclusion. Literature reviews on the relevant subject are also presented separately in each Chapter.

Chapter 2 presents the study on the influence of the substrate composition and surface crystallinity on the graphene growth. The preparation steps required to turn the copper catalyst ready for the CVD process are also discussed.

Chapter 3 demonstrates the graphene growth using the ethylene precursor gas. The experimental conditions used for the growth are explained in detail. Characterization methods are also mentioned, and results on partial and continuously covering graphene are presented.

Chapter 4 presents the study on the growth kinetics and the fundamental physicochemical mechanisms associated with the graphene growth on copper. First, the experimental conditions are detailed. Then, the results on the time-dependence of the graphene crystal enlargement are shown. The results are mathematically modeled and physically explained. Next, the thermal behavior of the graphene growth is presented. From the temperature-dependence, the activation energies are estimated for the rate-limiting mechanisms to be discussed. As the consequence, an overall picture of the graphene growth mechanisms is given at the end of this chapter.

Chapter 5 is focused on the morphology of the graphene crystals. A quantitative analysis of the crystal edges is detailed. Secondary layers and associated thermal behavior are presented, and the possible mechanisms for the secondary nucleations are proposed. The influence of copper sublimation on the crystal morphology is also investigated.

Chapter 6 shows the experiments on graphene transfer from the copper catalyst to insulating substrates. The early transfer method is introduced first, and then an improved method is presented. The advantages of the improved method are discussed. Lastly, results on the transfers to microporous substrates with a 100% yield are demonstrated.

This thesis is concluded in Chapter 7 by summarizing the results and findings. A concluding overview of the discussions is presented, followed by an outlook for future prospects of the field.

## Nomenclature

### *Abbreviations*

AFM	Atomic Force Microscope
APCVD	Atmospheric Pressure Chemical Vapor Deposition
CMOS	Complementary Metal-Oxide-Semiconductor
CNT	Carbon Nanotube
CVD	Chemical Vapor Deposition
DI	De-ionized
$E_A$	Activation Energy
EBSD	Electron Backscattering Diffractometry
HOPG	Highly Oriented Pyrolytic Graphite
I	Light Intensity of a Raman Spectrum
LEED	Low Energy Electron Diffraction
LEEM	Low Energy Electron Microscope
LPCVD	Low Pressure Chemical Vapor Deposition
PMMA	(poly methyl) methacrylate
SEM	Scanning Electron Microscope
TEM	Transmission Electron Microscope



## **2 Preparation for Growth: Substrate Effects on Graphene Quality**

Parts of this chapter have been published in:

K. Celebi, M. T. Cole, J. W. Choi, N. Rupeshinge, F. Wyczisk, P. Legagneux, J. Robertson, K. B. K. Teo and H. G. Park. Evolutionary Kinetics of Graphene Formation on Copper, *Nano Letters*, 2013, **13**(3): pp. 967-974.

Parts of this chapter have been submitted for publication in *CRC Handbook of Graphene Science*.

### **2.1 Abstract**

The role of a substrate is substantial in the graphene CVD, as it catalyzes the reactions that define the quality and morphology of graphene. When copper is used as the substrate material (*e.g.*, a copper foil), two properties of the substrate particularly influence the CVD process: (1) composition and (2) crystallinity of the foil. We have encountered different types of copper foils. Some of them, owing to impurities in their composition, are extremely difficult to produce graphene free of “white dots.” Other foils cause accumulation of amorphous carbon, possibly due to the coatings introduced in the foil production. We have also characterized the effect of artificial metal coatings and found that nickel can be a good material to alloy with copper in order to improve the graphene growth.

## 2.2 Introduction and Literature Review

The practically zero carbon solubility of copper [62] ( $10^{-3}$ – $10^{-2}\%$  for copper at 1000 °C) makes it an ideal catalyst to synthesize graphene. Surface catalysis and the lack of bulk-carbon cause the reaction to be self-terminating under particular growth conditions, yielding monolayer graphene [63].

If the substrate surface is rough, an initial chemical mechanical polishing step is often necessary [64]. Scratches and defects on the substrate could act as nucleation sites for the graphene synthesis, as illustrated in Figure 2.1. Smoother substrates have less nucleation sites, thereby reducing the nucleation density and enlarging the attainable grain size [65]. However, excessive polishing may disturb the spatial uniformity of the graphene grain sizes, as the nucleation sites are then non-uniformly distributed by the sparse defect sites. The resulting monolayer film can have poor grain connectivity, high sheet resistances consequently, and perturbed and undulating surfaces due to polishing [61].

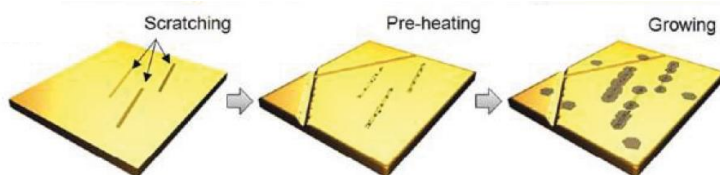


**Figure 2.1.** The demonstration of defects acting as nucleation sites. An increased nucleation density can be seen at the scratch-induced defect sites on the copper foil [65].

The next preparation step is reduction, often using acetic or hydrochloric acid pretreatments [66]. High-temperature annealing at 900-1000 °C is the main furnace process to remove the oxides on the surface right before the growth step. A commercial 25- $\mu\text{m}$ -thick copper foil can be reduced in 30 min, however the exact composition of the foil is also critical. Additional coatings or solvent impurities from substrate manufacturing processes may cause nanometer-sized particles to form during growth, which are visible under scanning electron microscope (secondary electron detection) [61, 67]. These

small particles are difficult to remove and can remain attached to graphene even after transferring to other substrates.

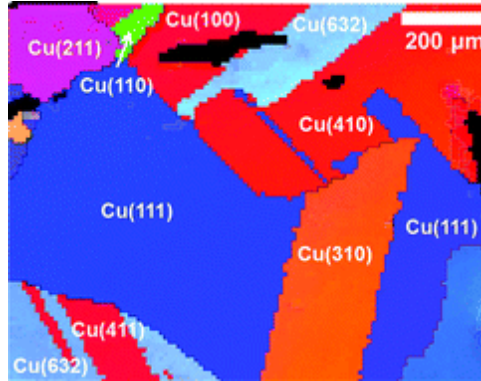


**Figure 2.2.** Crystalline orientation of the copper surface, as mapped by the electron back scattering diffraction [68].

Single or polycrystalline copper can be used for graphene growth [69]. The most popular forms of copper so far have been foils and thin films with polycrystalline morphology. The grain sizes of evaporation-deposited copper films can be increased from tens of nanometers to a few micrometers by annealing at 900-1000 °C [70]. This increase can be more dramatic in copper foils, sizing up to hundreds of nanometers [63]. Crystalline orientation is as important as the grain size for the growth and can be determined by electron back-scattering detection (EBSD), as shown in Figure 2.2 [68]. Annealing can also re-crystallize the surface, yielding mostly the identical crystalline orientation all over the surface [67]. For copper foils, EBSD maps show that the dominant surface orientation becomes (200); while for copper films, annealing crystallizes the mostly amorphous film to have a (111) surface [70]. Low-index copper facets is more likely to yield monolayer graphene with less defects [68]. It has been reported that copper films can produce higher quality graphene compared to foils [71]. Another factor that contributes to this quality is that higher hydrogen content of the films can replace the need of gaseous hydrogen for reducing the defect density [70].



## 2.3 Influence of Copper Foil Composition

### *Foil Contaminants*

A critical factor that influences the graphene quality is the copper foil composition. As the commercial foils used in graphene growth undergo rolling and other processing steps, additional contaminants and coatings can be present. These non-copper materials may cause drastic changes in the graphene morphology and surface cleanliness. Indeed, we have observed white dots, as described in the previous section, popping up on the surface after the growth on some copper foils. These particles could hinder the crystal enlargement and cause edge deformations as shown in Figure 2.3.

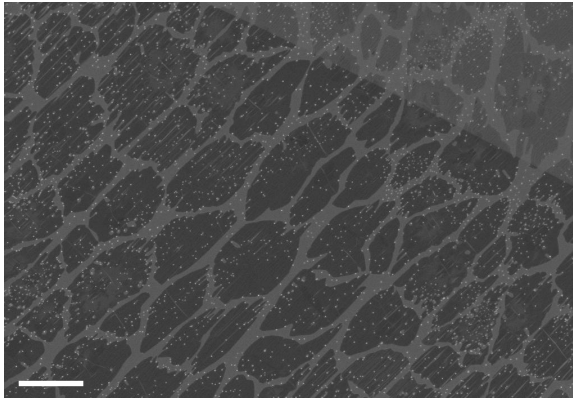


**Figure 2.3.** SEM image of the as-grown graphene on a copper foil. White particles are seen to hinder the graphene crystal enlargement, causing the shown finger-like crystal edges. The image is taken by an in-lens secondary electron detector. The scale bar is 2  $\mu\text{m}$ .

We performed Nano Auger analysis to understand the nature of these particles. The Auger analysis was carried out using a Physical Electronic PHI 680 Auger Nanoprobe with a multi-channel plate detector (in courtesy of F. Wyczisk and P. Legagneux). The kinetic energy of the incident electron beam was 5 keV, and the probe current was 10 nA. Under these conditions, the spot size less than 50 nm

allowed us to probe the elemental composition of points on the substrate. Nano Auger spectroscopy suggested that these dots are copper oxide and chlorine agglomerates, most likely a product of oxidation upon exposure to ambient air and surface pretreatment by standardized hydrochloric acid procedures during copper foil manufacturing (Figure 2.4). It remains for further investigation whether these particles also cause pinhole formation on as-grown graphene.

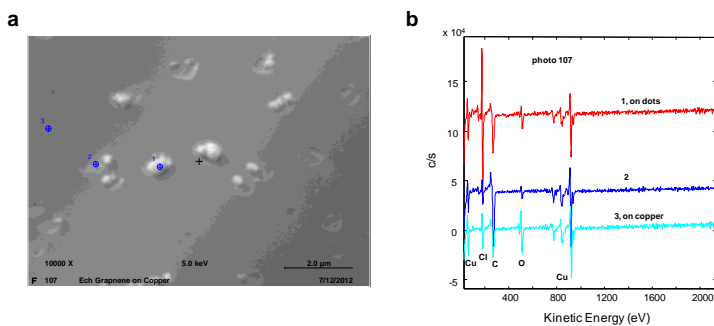


**Figure 2.4.** Nano Auger data on copper foils. (a) SEM image of the copper foil surface with small graphene crystals and white dots. (b) Nano Auger data corresponding to the blue-marked points on the left image. White dots on graphene crystals are shown to have significant chlorine and some carbon atoms (curve 1 - red). Graphene crystals have much less chlorine and similar amount of carbon atoms compared to the dots (curve 2 - blue), while copper without graphene covering have little carbon but some chlorine and a significant amount of oxygen due to the vulnerability to oxidation without the protective graphene covering (curve 3 - light blue). Chlorine atoms are often introduced during the production of the commercial copper foils.

### *Surface Coatings from the Foil Production*

Surface coatings on the copper foil can also influence catalysis on the surface. Most coated metals, such as molybdenum, can have orders of magnitude greater carbon solubility. Thus, dirt of amorphous carbon may form on the surface after the growth. Figure 2.5 shows dirty and

clean surfaces on different foil surfaces after the same growth.\* Another feature of this contamination is that the amorphous carbon chunks form preferably at the deep grooves of the copper foil, which may be due either to a higher defect density or to thicker metal coating at these sites.

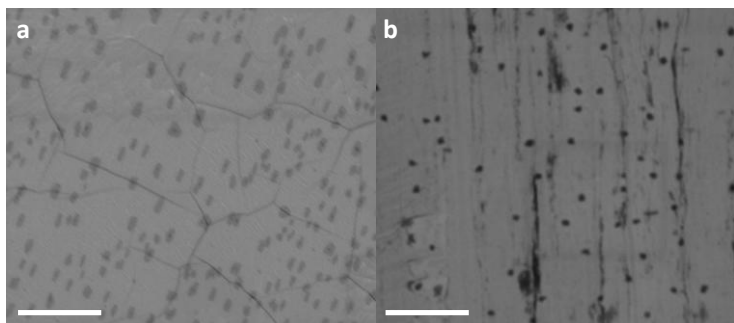


**Figure 2.5.** SEM images of the clean (a) and amorphous-carbon-contaminated (b) surfaces on different copper foils out of the same growth, performed at 950°C under a 50 sccm flow of ethylene for 2 minutes. The darker-gray regions on the left image indicate secondary layers and wrinkles, while the black regions on the right image show the amorphous carbon agglomerations. The scale bars are 2  $\mu\text{m}$ .

---

\* So far the best foil we have used is the old batch of Alfa Aesar's 25- $\mu\text{m}$ -thick copper foil (part # 13382)

## 2.4 Annealing and Surface Crystallinity

One critical factor for the uniformity of the graphene crystal morphology is the substrate crystallinity. The copper step morphology is dependent on the crystalline orientation, and thus the ripple formation on graphene is critically based on the crystallinity of the copper surface. We checked the surface crystalline orientation of the copper foils after the growth by EBSD. Unlike the surface structure in Figure 2.2, our copper surface consists of extremely large (mm-size) grains, which are (100) orientated (nearly parallel to the surface plane) independent of the growth temperature and time (Figure 2.6). Grain orientation maps display few grain boundaries but some lattice bending of  $ca. 10^\circ$  throughout the grains.

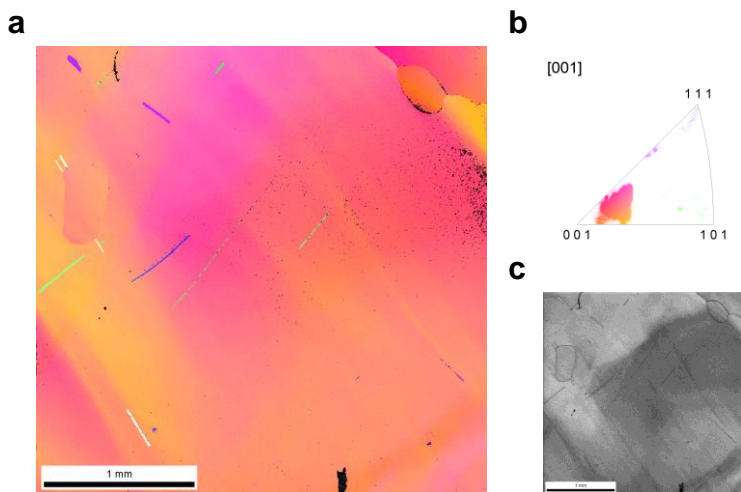


**Figure 2.6.** EBSD data on copper foil after growth. (a) Crystal orientation map with color table according to inverse pole figure with respect to the surface normal direction. (b) Inverse pole figure for the surface normal direction, implying the dominant copper crystallographic orientations in the map have (100) close to parallel to the surface plane. (c) Map of EBSD pattern sharpness, same area as shown in (a).

## 2.5 Additional Thin Metal Layers on Copper Foils

The influence of additional thin film metal coatings on the copper foil catalysts has been studied in order to see any possible improvement in the growth. Different thickness layers (10-100 nm) of nickel, gold and iron have been deposited onto copper foils by electron beam evaporation. The as-deposited foils and the bare copper foils then underwent the same growths for comparison. Figure 2.7 shows the SEM images of the as-grown graphene from the same growth process. No visible effect can be seen for the gold coating. For nickel coatings the average grain size clearly increases, however the morphology of the grains becomes more dendritic. Despite the worse morphology, nickel coatings can be a good improvement method for the copper-based growth of graphene. Indeed, there is a report demonstrating high quality graphene growth on copper-nickel alloys. For iron coatings, on the other hand, the growth is generally accompanied by the white-dot formation. These white particles have a different morphology than the particles originating from the control copper foil (as described before in this chapter). We attribute these white particles to the oxidation of iron during the transfer between e-beam deposition and CVD chambers. These particles can also hinder the enlargement of the graphene crystals and cause the crystal edges to become rougher. For thicker iron coatings (*i.e.*, 100 nm – not shown here) the resulting morphology is more dramatic, with no good graphene produced.

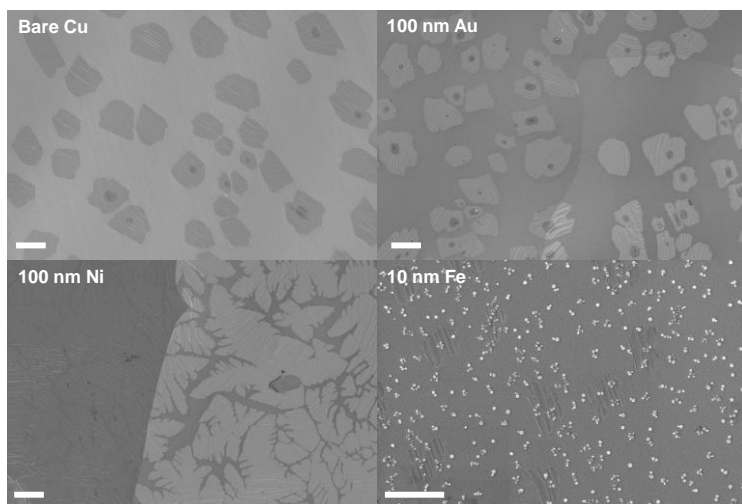


**Figure 2.7.** SEM images of the as-grown graphene on bare copper foil and thin-film-metal-coated copper foils. All images are from the same growth, which was performed at 900 °C under 7 sccm flow of ethylene for 5 minutes. The white scale-bars are 1  $\mu$ m.

## 2.6 Conclusions

Contaminants in the copper foils can result in the formation of oxide-like white particles, which could hinder the growth locally and modify the graphene crystal morphology with increasing the edge-to-area ratio. Coatings introduced to the copper foils during the production can cause amorphous carbon agglomeration, making the graphene dirty in the end. So a careful selection of the copper foil (*i.e.*, the old batch of Alfa Aesar's #13382 copper foil) is critical in achieving good graphene synthesis. Further trials by additional deposition of gold have not caused any visible change to the end product, while additional iron layers produced oxide particles that hindered the graphene enlargement. Meanwhile, additional nickel layers have shown promising results despite the worse crystal morphology. This effect can be a subject of future study to reduce the growth temperatures on copper foils.





### 3 Growth Conditions and Characterization of the Graphene

Parts of this chapter have been published in:

K. Celebi, M. T. Cole, K. B. K. Teo and H. G. Park. Observations of Early Stage Graphene Growth on Copper, *Electrochemical and Solid-State Letters*, 2012, **15**(1): K1-K4.

K. Celebi, A. O. Altun, K. B. K. Teo and H. G. Park. Observation of the Graphene Surface Structure at the Early Stages of Graphene Growth on Copper, *ECS Transactions*, 2011, **35**(3): pp. 147-159.

K. Celebi, M. T. Cole, J. W. Choi, N. Rupeshinge, F. Wyczisk, P. Legagneux, J. Robertson, K. B. K. Teo and H. G. Park. Evolutionary Kinetics of Graphene Formation on Copper, *Nano Letters*, 2013, **13**(3): pp. 967-974.

#### 3.1 Abstract

In this chapter we report our observation of graphene growth based on an ethylene-based CVD method, capable of reducing the growth temperature to below 800 °C for monolayer graphene growth on copper films and foils. We track the early stages of slow growth under low partial pressures of ethylene and observe the partial graphene covering by SEM and Raman spectroscopy. We find that the edge states contribute to the defect modes to modify the Raman spectra. We also investigate the surface energy of the partially grown graphene and demonstrate that the hydrophobicity can be fine-tuned by controlling the initial growth of the graphene domains. Finally, continuous graphene monolayer growth is obtained and quality-checked. The continuous monolayer graphene accounts for over 98.4% of the measured area ( $I_G/I_G = 1.82 \pm 0.25$  ( $\pm 1$  S.D.)), with the remaining area being mostly bilayer. The measured electron mobility of  $3,600 \text{ cm}^2\text{V}^{-1}\text{s}^{-1}$  also supports the low defect density we observed.

## 3.2 Introduction

A typical growth on copper starts with conditioning of the substrate to reduce the oxides on the surface by high-temperature annealing (*i.e.*, 900-1000 °C), followed by exposure to the carbon precursor (*i.e.*, methane) at the similar temperatures. The graphene nucleates and enlarges by consuming the reactants catalyzed on copper from the carbon precursor. Although the available parametric window for continuous monolayer synthesis is wide [72] (*i.e.*, for methane: 800-1050 °C, 0.01 mTorr - 760 Torr), the variation of the morphology by the growth parameters can cause important variations in its physical properties.

So far several groups have used methane as a carbon precursor for the surface catalysis process on copper [63, 66, 73-75]. As shown in the CVD growth of CNTs, methane is cleaner than other conventional carbon precursors [76], but it requires higher temperatures for pyrolysis compared to other precursor gases such as acetylene or ethylene. Being more reactive and able to synthesize carbon nanomaterials at much lower temperatures, acetylene can easily lead to deposition of undesired amorphous carbon and degradation of the nanomaterial quality [77]. This degradation, however, can be controlled by the use of atomic hydrogen, which suppresses the decomposition of acetylene and ethylene [76, 78] and etches away the amorphous carbon deposits [79]. Although these two properties of hydrogen can improve the quality of the graphene, it can also have a detrimental effect of transforming the  $sp^2$  bonds into  $sp^3$  [80]. Thus, the hydrogen flow rate must be carefully chosen in using these carbon sources. An example of this graphene growth by CVD using acetylene has been demonstrated on copper films at a lower temperature, albeit with a large Raman D-mode intensity [77]; indicating the difficulty in controlling the amorphous carbon deposition by acetylene pyrolysis. Compared to acetylene, however, ethylene has a lower reactivity [81, 82] and promises an easier control for the lower temperature growth on copper.

### 3.3 Materials and Methods

#### *Growth conditions*

All of our ethylene-based growths were carried out in a cold-wall, vertical-flow CVD system (*Black Magic*<sup>TM</sup> CVD System by Aixtron, Figure 3.1). As a copper substrate to grow graphene on, we employed copper foils (Alfa Aesar, 25  $\mu\text{m}$  in thickness and 99.8% in purity). For a typical process at 4.1 mbar and 850  $^{\circ}\text{C}$  (Figure 3.2), native oxides on the copper foils are reduced under a 20-sccm flow of hydrogen diluted by 1500 sccm of argon, for 30 min (including a 5-min temperature ramp from room temperature to 850  $^{\circ}\text{C}$ ). Reduction is followed by a 10-min graphene growth at the same temperature with an addition of 7 sccm of ethylene without altering the other gas flows. The ethylene flow is stopped immediately before the cooling step, so as to prevent precursor pyrolysis at lower temperatures. Hydrogen and argon flows continue until the temperature reaches 400  $^{\circ}\text{C}$ , and then the system further cools down below 100  $^{\circ}\text{C}$  in an argon only environment. The temperature, temperature ramp, pressure and flow rates were controlled by a software interface. A heated graphite stage provided the heating without heating the entire chamber: a cold-wall reactor. We measured and controlled the sample substrate temperatures by use of an infrared temperature sensor.



**Figure 3.1.** The cold-wall, vertical-flow CVD system by Aixtron, AG. All growths in this work have been performed by use of this system.

### *Characterization Methods*

The synthesized graphene were characterized by Raman spectroscopy, a widely used non-destructive technique that quantifies the defect density and crystallographic quality of carbonaceous products [83]. Raman measurements were performed by use of 532-nm excitation (2 mW) with a focal spot size of *ca.* 0.4  $\mu\text{m}$  (WiTec CRM 200) and a 457-nm excitation (3 mW) with a spot size of *ca.* 1.2  $\mu\text{m}$  (Renishaw inVia). The surface morphology was characterized by field emission scanning electron microscopy (Zeiss Gemini 1530 FEG) to image the as-grown graphene films on the copper foils, as well as Raman spatial mapping of transferred graphene samples on silica using 532-nm excitation.

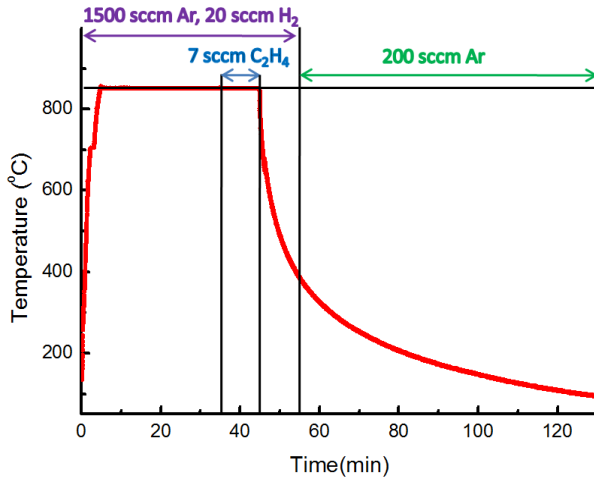


**Figure 3.2.** A typical recipe used for graphene growth on copper foils. The chamber is always loaded/unloaded below 100 °C, to prevent the copper oxidation.

### 3.4 Results and Discussion

#### *Raman Spectroscopy on Copper*

Metal substrates that catalyzed graphene growth usually have surface roughness and a strong fluorescence background (Figure 3.3, inset), which impedes the correct characterization of as-synthesized graphene. In order to avoid this difficulty, we transferred the graphene films onto a flat, less spectrally overlapping substrate such as silica in two different ways. Initially, we tried to etch away the copper in a 1-M  $\text{FeCl}_3$  solution and then fish out the freely floating film of graphene from top of the solution by a silica substrate. This method was successful in transferring rather thick, multilayered graphene.

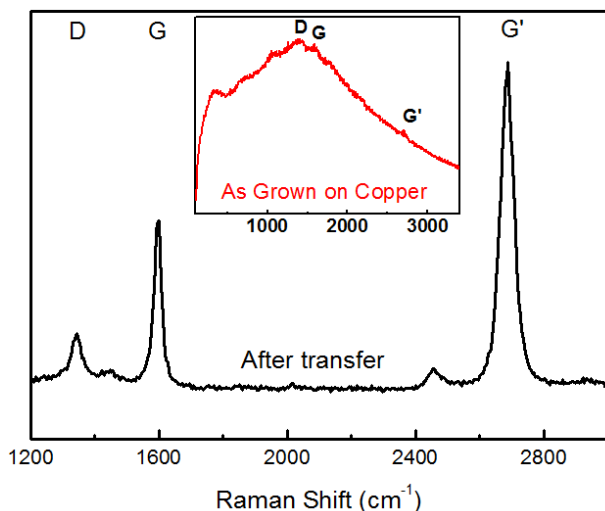


**Figure 3.3.** Raman spectrum of the transferred graphene (on silica/silicon substrate) grown according to the recipe shown on Figure 3.2. *D*, *G* and *G'* denotes the corresponding Raman bands. The Raman spectrum of the as-grown graphene on the copper foil is shown in the inset figure.

However, as the synthesized graphene nears mono- or a very few layers, we find it difficult to transfer the graphene with this method because the surface tension or the lateral flows of the thin liquid film between graphene and the pulling substrate can destabilize and tear apart the floating graphene layers. Slight reduction of surface tension through dilution of  $\text{FeCl}_3$  did not help avoiding the destabilization. Thin films of poly-methyl methacrylate (PMMA) [84] finally enabled the stable transfer of graphene. The PMMA (4% in ethyl lactate) was spun on the graphene-coated copper foil at 4000 rpm for 30 sec, followed by a 1-min bake at 180 °C. Etch of the copper in the 1-M  $\text{FeCl}_3$  solution for one hour left the PMMA-graphene layer floating on the surface of the etchant solution. After rinsing this layer in DI water we pulled it out with the silica substrate with the PMMA side facing up. Finally, removal of PMMA by acetone and isopropanol rinses exposed the graphene layer on top of the silica substrate.

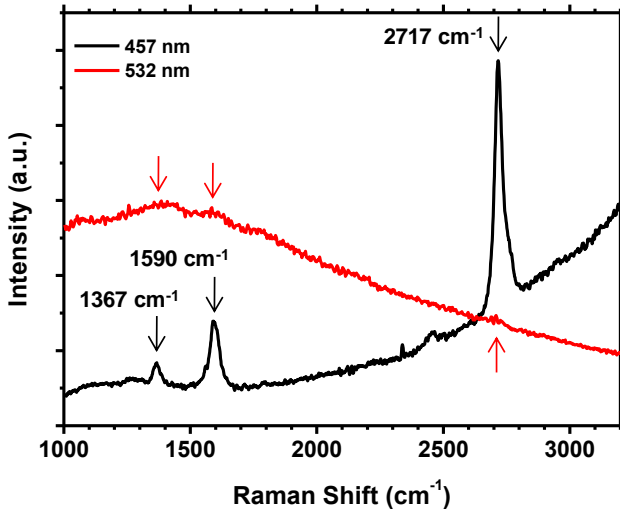


**Figure 3.4.** Comparison of the Raman spectra taken on the as-grown graphene on a copper foil using 457-nm (black curve) and 532-nm excitations (red curve). The arrows indicate the major Raman *D*, *G* and *G'* peaks, from left to right, respectively.

Alternatively, the use of shorter wavelengths can reduce the fluorescence background from copper. Indeed, a blue laser at 457 nm significantly improved the Raman spectrum compared to the 532 nm laser. Figure 3.4 shows the difference between these two wavelengths. Both spectra were taken from as-grown graphene on copper foils.

### *Characterization of Graphene Crystals*

In order to be able to capture the partial covering by structurally simpler and smaller domains at the very early stages of the graphene growth, we used a low flow rate and partial pressure of ethylene and varied (1) the growth time while keeping the temperature at 850 °C or (2) the temperature while keeping the growth time at 5 minutes. We confirmed this partial graphene covering by small domains by taking the AFM and SEM images. The progress of this incomplete covering over time and temperature is shown by the SEM images of the as-grown graphene on copper foils (Figure 3.5). We observe that the graphene domain size increases non-linearly by increasing the growth time from 1 min to 30 min. We also see a similar trend of enlarged graphene domains by the growth temperature increasing from 800 °C to 950 °C, which is attributed to an increase in the graphene growth rate. Another important finding is that the graphene domain density decreases as the growth time increase. This decrease can be attributed to the interconnection of the small domains; however, the spacing in between the domains increases until the 10-min growth, which hints about a possible migration of the graphene domains during the growth at high temperature. More detailed results and discussion on the partial growth and the evolution of the graphene crystals can be found in the next chapter of this thesis.

The Raman spectroscopy analysis quantitatively bolsters the SEM observations. Figure 3.6 shows the Raman spectra of the graphene films (transferred to silica) grown at different temperatures and for various durations. All the spectra show the three major Raman peaks: *D*, *G* and *G'*. The *G'* band is key in determining the film thickness, since this band originates from a double resonant process involving the generation of an electron-hole pair, a splitting in the electronic bands caused by interlayer coupling in multilayer graphene induces a deviation from the single Lorentzian behavior [81, 83].



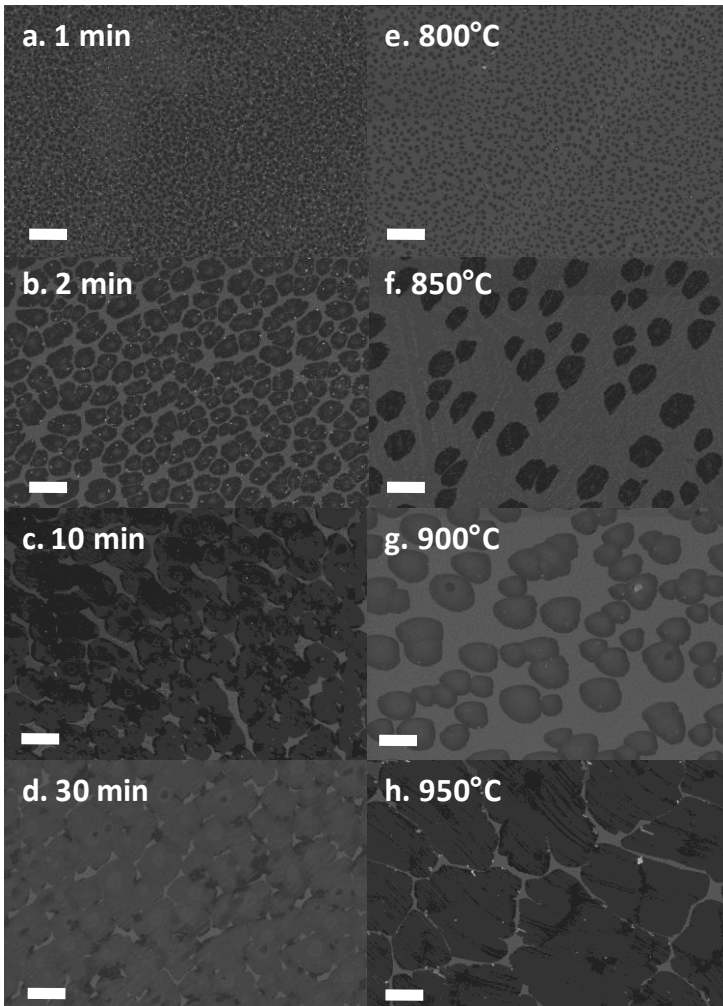


**Figure 3.5.** SEM micrographs of as-grown graphene on Cu foils. (a-d) Grown at 850°C for: 1 min (a), 2 min (b), 10 min (c) and 30 min (d). (e-h) Grown for 5 min at: 800 °C (e), 850 °C (f), 900 °C (g) and 950 °C (h). Dark regions correspond to the graphene domains. (2 $\mu$ m scale bar)

The standard interpretation here is that a single-Lorentzian-fitted  $G'$  peak indicates monolayer graphene [83]. Since a single consideration of the shape of the  $G'$  peak may be somewhat misleading for thick, turbostratically ordered multilayer graphene with subsequent electronic decoupling [85], it is important to examine the  $G'$  peak position and intensity as well. Indeed, the peak position ( $2690\text{ cm}^{-1}$ ) and high intensity both strongly supported the monolayer nature of our graphene crystals [40, 81, 83]. The low-intensity of the  $D$  peak also indicates a rather low-defect density in the basal plane. The positions of the  $D$ ,  $G$  and  $G'$  peaks are  $1350\text{ cm}^{-1}$ ,  $1590\text{ cm}^{-1}$  and  $2690\text{ cm}^{-1}$ , respectively, for the 532-nm excitation and around  $1366\text{ cm}^{-1}$ ,  $1590\text{ cm}^{-1}$  and  $2725\text{ cm}^{-1}$ , respectively, for the 457-nm. The shifts in  $D$  and  $G'$  peak positions are caused by the peaks' dispersive nature [86]. The small domain samples (800 °C and 1-min grown samples) show more prominent  $D$  peaks and three additional disorder-oriented peaks at  $1450\text{ cm}^{-1}$ ,  $1620\text{ cm}^{-1}$  ( $D'$ ), and  $2900\text{ cm}^{-1}$  ( $D+D'$ ) during 532-nm excitation. These features are attributed to incomplete crystallization and edge-state dominance at this very early stage nucleation.

The  $D/G$  and the  $G'/G$  intensity ratios are plotted in Figure 3.7. For samples with small domains the intensity of the  $D$  peak is large and there is a clear trend of decreasing the  $D/G$  intensity ratio by increasing domain sizes. We attribute this effect to the incomplete covering of the surface by graphene and the resulting abundance of domain edges. These edges may act as defects or phonon scattering sites that leave fingerprints as the Raman  $D$  band. The  $D$  peaks for the higher-temperature or longer growth-time samples are greatly reduced due to the greater covering of the surface by graphene and the suppression of the number of edge atoms.  $D'$  and  $D+D'$  peaks are also not visible for these samples. Indeed, the intensity increase in the  $D$  peak and other disorder-oriented peaks has also been observed by other groups for the partial monolayer coverage of the sample surface by graphene [87, 88]. The other clear trend in Figure 3.7 is that the  $G'/G$  intensity ratio also increases in proportion to time and temperature. The lower Raman  $G'$  intensity has been used to indicate the existence of thicker graphene [81, 83]. This understanding, however, cannot explain our observation because the graphene cannot be thick in the beginning and become thinner by increased growth time or temperature. Therefore, we attribute the increase in

$G'/G$  intensity ratio to the increased graphene domain size and the decreased number of edge atoms [87].

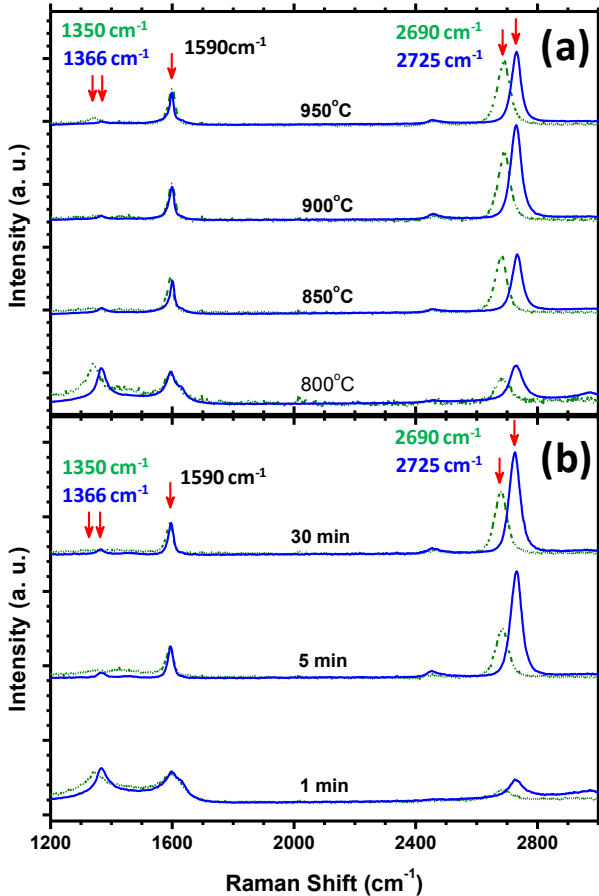


**Figure 3.6.** Raman spectra of a time series (a) and temperature series (b). Green (blue) curves show the Raman data for the 532-nm (457-nm) excitation. For the time series the temperature was maintained constant at 850 °C, and for the temperature variation the growth time was maintained constant at 5 min.

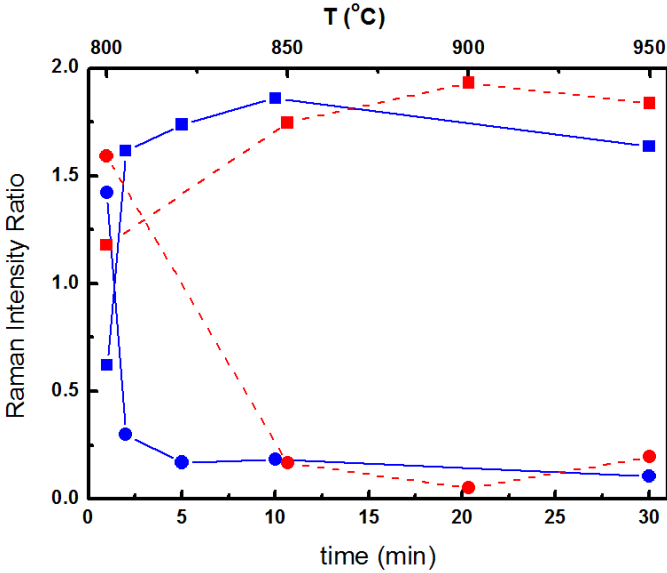


**Figure 3.7.** Peak intensity ratios for the Raman spectra shown in Figure 3.6. Blue data stands for the time variation (bottom axis) and the red data stands for the temperature variation (top axis). Rectangles show the Raman  $G'/G$  intensity ratio and circles show the Raman  $D/G$  intensity ratio.

Finally, in order to investigate the hydrophobic nature of a graphene-coated surface, we carried out contact angle measurements of the as-grown graphene on copper. Figure 3.8 shows the images of water droplets under static conditions at ambient pressure and room temperature. The samples have graphene grown at 800 °C, 850 °C, 900 °C, and 950 °C. From the density functional theory calculations, it is found that interaction energy between graphene and water is one-order-of-magnitude weaker than that among water molecules at bulk [89]: graphene is hydrophobic. Since the graphene covering on copper enlarges by temperature, we expect that the contact angle should increase for higher temperature samples. Indeed, as the graphene covering increases, so does the contact angle: 85° for the bare copper film with possible native oxide, then 88° for the 800 °C and 92° for the 850 °C samples to 95° for the 900 °C and 102° for the

950 °C samples. Another contributing effect on the hydrophobicity is the edges of graphene domains that we believe promote the surface wetting. Our samples show that, as graphene extends over the copper surface, the total boundary line of the graphene decreases. Cosine value of the contact angle, which represents the degree of liquid wettability according to Young's equation, is found linearly proportional to the total boundary line. From these observations, we attribute the diminution of surface hydrophobicity to both increase in edge carbon atoms and decrease in the basal plane carbon atoms of the graphene domains. The detailed effect of edge and basal-plane carbon atoms remains to be further investigated.

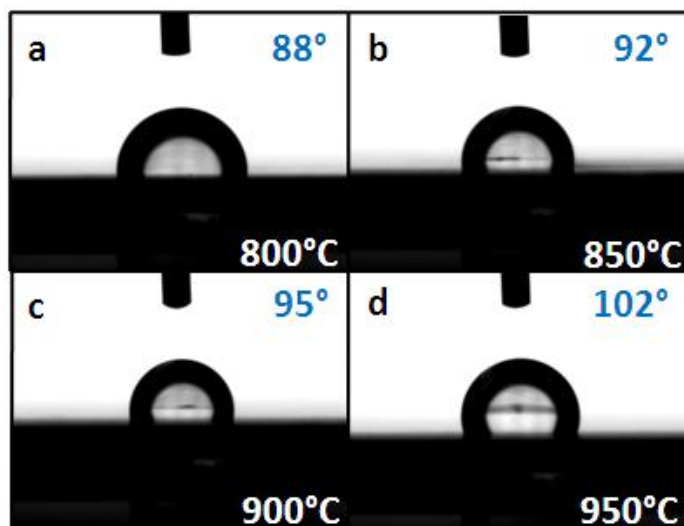


**Figure 3.8.** Images of the still water droplets on as grown graphene on copper film (a-d) at 800 °C (a), 850 °C (b), 900 °C (c), 950 °C (d). Numbers on the top denote the corresponding contact angles for the droplets. The contact angle for bare copper film is 85° (not shown here).

We rule out the effect of the copper substrate roughness on the hydrophobicity as we observe the increase in the contact angles by improved covering [90]. We believe it is rather the interaction of water with carbon atoms on the surface that governs the hydrophobicity. Indeed, the theoretical models, which take the dipole

charge effects of water [91] into consideration predict that the contact angle for graphene would be around  $95\text{-}110^\circ$  [92, 93]. Our contact angle measurements also suggest that the graphene is not extremely hydrophobic; yet this could actually be advantageous for nanofluidic applications in which the hydrophobicity can play a crucial role in water transport enhancement through a balance between entrance impedance and minimized friction [94].

### *Characterization of the Continuous Graphene*

Figure 3.9 shows an SEM micrograph of a continuous monolayer showing small ( $< 1 \mu\text{m}^2$ ) hexagonal secondary crystals, which will be discussed in further detail later. Secondary layer formation was also confirmed by detailed Raman analysis (Figure 3.9). Monolayer graphene accounts for over 98.4% of the measured area ( $I_G/I_G = 1.82 \pm 0.25$  ( $\pm 1$  S.D.)), with the remaining area mostly bilayer. Spatially resolved Raman spectra over  $150 \mu\text{m}^2$  show bilayer regions (blue) in addition to sub-micron juvenile bilayers (green). Interestingly, negligible defects were observed across the measured area, even at the edges of these bilayer regions, with an  $I_D/I_G$  of  $0.09 \pm 0.02$  ( $\pm 1$  S.D.) The measured electron mobility of  $3,600 \text{ cm}^2 \text{ V}^{-1} \text{ s}^{-1}$ , suggesting high quality graphene, also supports the low defect density observed here.

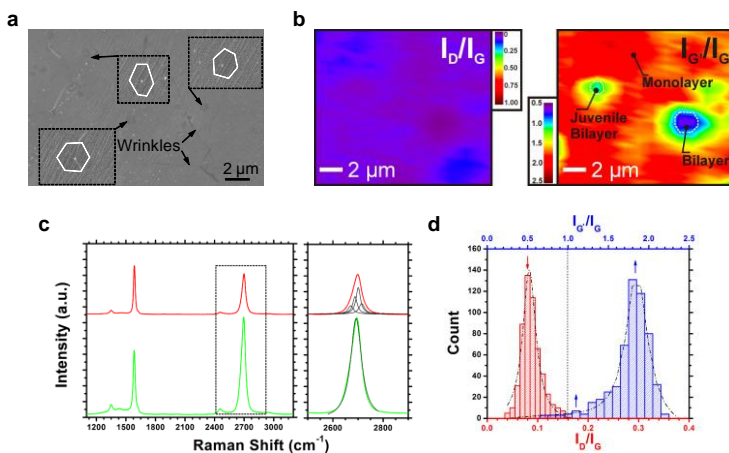


**Figure 3.9.** An SEM micrograph of a continuous monolayer. Small secondary layers are magnified to illustrate the hexagonal crystal morphology. White lines are drawn at the secondary layer boundaries for visual guidance. (Scale bar: 2  $\mu\text{m}$ ) **(b)** Raman map of the  $I_G/I_G$  and  $I_D/I_G$  showing monolayer (red), juvenile bilayer (green) and bilayer (blue) regions (Scale bar: 2  $\mu\text{m}$ ). **(c)** Typical 532 nm Raman spectra of a monolayer (green) and bilayer (red) regions with single and fourfold Lorentzian fits to the  $G'$  peak (2690  $\text{cm}^{-1}$ ) **(d)**  $I_D/I_G$  (0.09 $\pm$ 0.02) and  $I_G/I_G$  (1.82 $\pm$ 0.25) distributions.

### 3.5 Conclusions

We have demonstrated the use of the ethylene precursor in the CVD growth of graphene on copper foils. Our *ex-situ* observation of the partial covering of the copper surface by small graphene domains grown by short-time CVD runs at varied temperatures provides evidence of the lateral surface-catalyzed growth mechanism during the early stage of growth. Temperature has also been shown to increase the growth rate and decrease the final domain density. Continuous covering of graphene has also been achieved and characterized. Monolayer graphene accounts for over 98.4% of the measured area ( $I_G'/I_G = 1.82 \pm 0.25$  ( $\pm 1$  S.D.)), with the remaining area being mostly bilayer. The electron mobility of this layer is measured to be  $3,600 \text{ cm}^2 \text{ V}^{-1} \text{ s}^{-1}$ .

Using the partially covered samples, we also have shown that graphene is indeed hydrophobic, but not superhydrophobic. Through graphene coatings, we envision that a sub-molecular-level smooth surface can be manufactured and that the hydrophobicity of the surface can easily be tuned by, for example, the topological control of the surface covering by graphene. We believe that the understanding and control of the surface hydrophobicity by a graphene covering pose a great potential in making scalable and low-cost hydrophobic coatings and novel micro-nanofluidic devices.





## 4 CVD Kinetics and Fundamental Mechanisms that Govern the Growth

Parts of This chapter have been published in:

K. Celebi, M. T. Cole, J. W. Choi, N. Rupeshinge, F. Wyczisk, P. Legagneux, J. Robertson, K. B. K. Teo and H. G. Park. Evolutionary Kinetics of Graphene Formation on Copper, *Nano Letters*, 2013, **13**(3): pp. 967-974.

K. Celebi, M. T. Cole, N. Rupesinghe, P. Greenwood, L. Tao, D. Akinwande, J. Robertson, H. G. Park and K. B. K. Teo. (Invited) Growth Kinetics and Uniform Scaling-up of Graphene Synthesis, *ECS Tansactions*, 2013, **53**(1): pp. 17-26.

Parts of this chapter are due to be submitted for publication in *CRC Handbook of Graphene Science*.

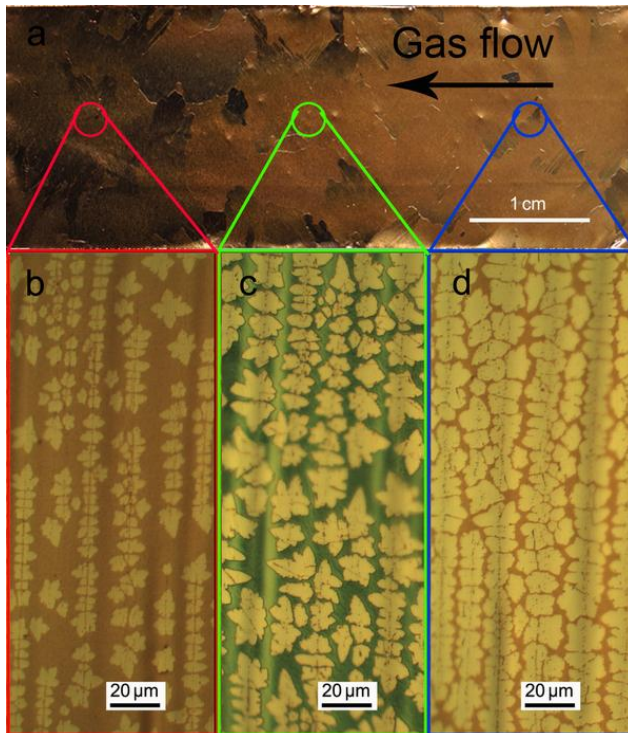
### 4.1 Abstract

It has been claimed that graphene growth on copper by CVD is dominated by crystallization from the surface initially supersaturated with carbon adatoms, which implies that the growth is independent of hydrocarbon addition once graphene is nucleated. Here, we present an alternative growth model based on our observations that oppose this claim. Our Gompertzian sigmoidal growth kinetics and secondary nucleation behavior support the postulate that the growth can be controlled by adsorption-desorption dynamics and the dispersive kinetic processes of catalytic dissociation and dehydrogenation of carbon precursors on copper.

## 4.2 Introduction

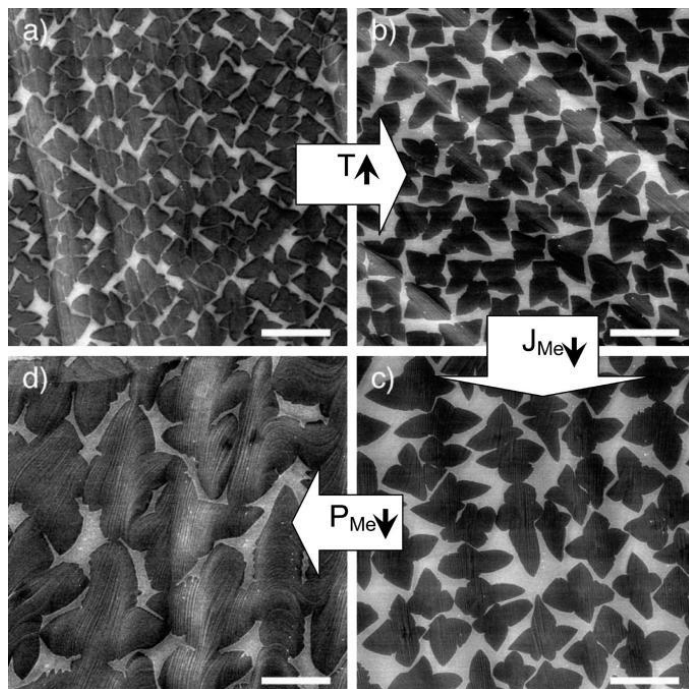
### *Nucleation of Graphene on Copper*

Most carbon precursors, such as methane, acetylene and similarly reactive hydrocarbons, readily chemisorb onto faceted copper surface and face only a comparatively small energy barrier on the order of 0.1 eV [95]. As the adsorbed carbon species, albeit unknown in the form, populate the surface and subsurface, supersaturation is reached.



**Figure 4.1.** Demonstration of the influence of the carbon precursor partial pressure on the areal density of the graphene flake nucleation. As the gas flows through the copper foil, the hydrocarbons are consumed, reducing the partial pressure in the downstream. Images are taken by optical microscopy [96].

The surface defects then act as sites triggering heterogeneous nucleation. An evidence of the defects acting as nucleation sites can be seen on the scratch site in Figure 2.1 [65]. Immediately following the initial nucleation these graphene seeds begin to deplete the nearby solid solution of carbon reactants. The form of these reactants is disputed, with indications ranging from carbon adatoms [61] to carbon clusters [97] or even hydrocarbons [95, 98]. As the nucleation is governed by the initial carbon supersaturation of the catalyst and the availability of suitable lattice defects, the hydrocarbon partial pressure and the catalyst temperature define, in part, the spatial number density of the nucleation events.



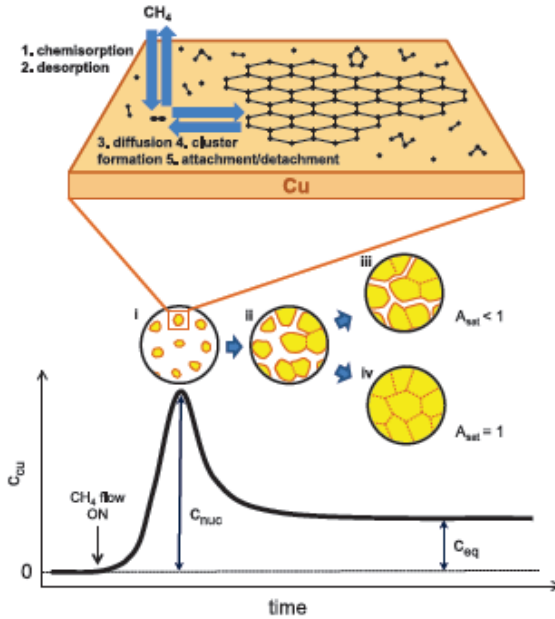
**Figure 4.2.** SEM images of the graphene flakes grown at different conditions. The arrows indicate the relative change of the growth parameters. The decrease in the areal density of the nucleation events follows the arrows, indicating the role of the associated parameters on graphene nucleation density [58].

Figure 4.1 shows a reduction in the nucleation density due to depletion of the available methane gas, which reduces the number of available supersaturated carbon reactants at the moment of the seeding event [96]. Any disturbances in the flow by edge may also cause inhomogeneities in the nucleation distribution, which can be critical in the horizontal-flow CVD furnaces. The SEM images of Figure 4.2 indicates that the nucleation density is proportional with decreasing temperature and increasing hydrocarbon partial pressure and flow rate [58]. Temperature also defines the amount of supersaturation. The capture and desorption of the carbon reactants are highly dependent on the temperature [99]. It has also been reported that at lower CVD temperatures the nucleation is limited by the capture events of the reactants with an activation energy ( $E_A$ ) of *ca.* 1 eV, while at higher temperatures desorption becomes the dominant mechanism and governs the nucleation with a higher  $E_A$  of *ca.* 3 eV [61].

### *Graphene Growth Kinetics*

The time dependence of the growth rate is critical to understand the fundamental mechanisms that govern the CVD of graphene. The information about the growth rate can be extracted by observing the variation in graphene flake size over the growth time. Studies on Ru-based growth by real-time observation using low energy electron microscopy (LEEM) have been presented [44, 100], however it is challenging to employ this technique for copper due to lower carbon density and substrate sublimation [44, 101]. As such the literature on the copper-based CVD kinetics is, at present, rather limited. Recently, methane-based graphene CVD investigations by Kim *et al.* have proposed a supersaturation-driven growth, a claim that attributes the entire growth to depletion of the initial population of the carbon adatoms from the surface (Figure 4.3) [61]. In this work, an exponential-like kinetics curve was fitted by the Johnson-Mehl-Avrami-Kolmogorov (JMAK) crystallization model [102], with the assumptions of instant nucleation and carbon-attachment-limited growth, where they incorrectly neglected any contribution of the additional hydrocarbon input during the growth. Their fitting implied that the growth saturates and a continuous graphene layer can never be achieved unless there is sufficient carbon source available at the

initial growth stage. Based on similar assumptions, the continuity of the graphene layer can be modeled as a function of the ratio of the methane partial pressure to the square of the hydrogen's pressure:  $P_{\text{CH}_4}/P_{\text{H}_2}^2$ . Growth continuity is achieved for partial pressure ratios of  $> 0.01$  for growth temperatures greater than  $900\text{ }^\circ\text{C}$  [103].



**Figure 4.3.** Illustration of the graphene growth based on the carbon adatom attachment. Bottom: the density of the carbon adatoms versus time. Here an initial supersaturated state is depleted by the enlarging graphene crystals [61].

### Reaction Energetics

Determination of the reaction energetics is critical in order to determine the rate-limiting processes during CVD growth. The associated energy barrier of each of all the possible reactions determines the importance of each step in the overall potential

scheme. Prior to any of these steps, when the hydrocarbon feedstock is introduced, gas-phase reactions occur prior to adsorption [104]. However, unlike the rich literature on the gas phase reactions involved in carbon nanotube growth often employing *in-situ* mass spectroscopy [105-107], analogous studies for probing the growth atmosphere during graphene growth do not abound. Moreover, since the adsorption energy barrier of most hydrocarbons on Cu is negligible (approx. 0.1 eV) [95], any transiently derived  $C_xH_y$  species formed in the gas phase rapidly adsorb, disabling direct measurement and contributing to the complexity of the underlying catalytic reactions. Moreover, thermal variations with CVD reactors only support the formation of such transients in hot zones particularly, further complicating direct measurement. Currently very little is known about these hydrocarbon reaction cascades on copper. Consequently, it is very difficult to make any assertions on the effects of gas phase reactions on the overall CVD process.

Carbon reactant diffusion follows hydrocarbon adsorption [108, 109]. The energy barrier for diffusion is also low, typically less than 1 eV for copper [95, 109]. Thus, under equilibrium conditions diffusion is rather unlikely to be a rate-limiting step. However, it may become dominant under certain conditions, in particular when the hydrocarbon reactions are simpler and diffusion occurs at the subsurface. Nie *et al.* have concluded that diffusion is the likely rate-limiting mechanism when pure carbon is used as the precursor on copper (111) surfaces under ultrahigh vacuum conditions [101]. Besides surface diffusion, gas-phase diffusion is also important under APCVD (Figure 4.4) [110]. During APCVD a boundary layer forms at the substrate surface, and gas diffusion through this boundary becomes rate limiting. Care must be taken when extracting the activation energies from the resultant Arrhenius curves. To conclude the correct energy barriers responsible for chemical processes, this kind of mass-transport-limited regime must be ruled out.

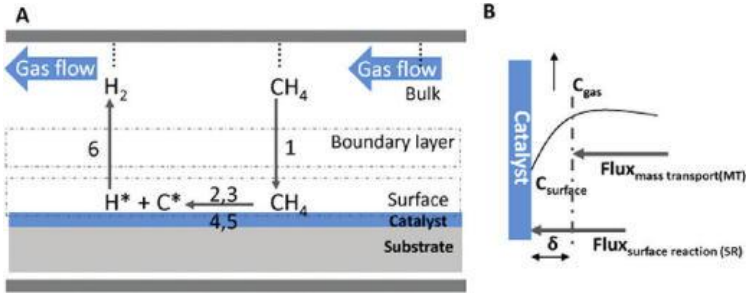


**Figure 4.4.** (a) Illustration of the processes for graphene growth on low-carbon-solubility catalysts. (1) Diffusion through the boundary layer, (2) adsorption onto the surface, (3) hydrocarbon decomposition, (4) surface diffusion, (5) desorption, (6) diffusion of desorbed species through the boundary layer. (b) Illustration of the steady state mass transport [110].

When gas phase hydrocarbon transport is not the limiting factor, the catalyzed physicochemical reactions on the copper surface determine the rate of graphene crystal enlargement rate. Two main reaction types occur on the surface: (1) a dehydrogenation cascade, which may also involve dissociation of the radicals depending on the carbon precursor, and (2) attachment of carbon in the form of adatom, chain/cluster or hydrocarbon at the crystal edges of growing graphene. The exact nature of these reactions is not clear. A simplistic diagram that displays the approximate energy levels of the adsorption and dehydrogenation is shown in Figure 4.5 [111]. The dehydrogenation energy barrier indicates that the overall reaction is unfavorable and must be supported by excessive hydrocarbon feed. This finding also suggests that reactive precursors can be used for graphene growth at lower temperatures, as once these gases are adsorbed, desorption becomes more difficult.

When the complete process of flake formation is considered the rate-limiting reaction is disputed. Accurate measurement of  $E_A$  is required for the determination of the reaction that determines the growth speed. For a methane precursor, Kim *et al.* have found an  $E_A$  of 2.6 eV [61], concluding the carbon adatom attachment (*ca.* 2 eV energy barrier) [44] to be the rate-limiting step, with the claim that the dehydrogenation energy barrier is lower (1.7-1.9 eV) [112, 113]. The



species that attach to the flake edges are also widely debated. While some reports focus on the adatoms [61, 103, 114], there are also reports that compare different species and conclude that few-atom carbon chains are also important reactant species [97]. An increase in the CVD pressure has also been claimed to favor carbon chains versus adatom formation [115].

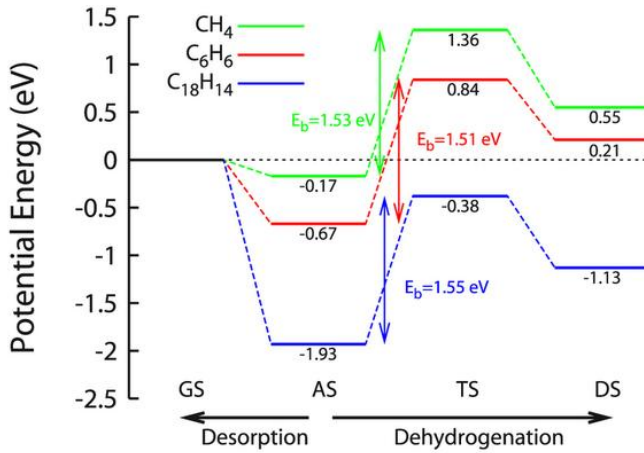


**Figure 4.5.** Energy diagram illustrating the energy levels of the different states of various hydrocarbons: gas state (GS), adsorbed state (AS), temporary state (TS) and dissociated state (DS)[111].

### 4.3 Experimental Methods

For ethylene-based CVD, copper foils (99.8%, Alfa Aesar) were first reduced at 900 °C (measured by an infrared pyrometer and bimetallic thermocouples) at an initial thermal ramp rate of 300 °C/s, under 20 sccm of hydrogen (99.999%), diluted by 1500 sccm of argon (99.999%) for 30 min. This annealing procedure was consistent for all to ensure that all growths initiate on comparable copper grain sizes (some mm in diameter) and crystallographic orientations (Cu(100)) [116]. After 2 min of thermal re-stabilization, 7 sccm of ethylene (99.999%) was introduced to the hydrogen-argon atmosphere to initiate graphene growth, over 0.5-4 min at varied temperatures. Ethylene flow was stopped immediately prior to chamber cooling (Figure 4.6a). Hydrogen flow was maintained until <400 °C to prevent copper oxidation that may occur as a result of trace amount of oxygen present within the chamber (verified by *in-situ* mass spectrometry, Figure 4.6b). According to our control experiments, 20 sccm of hydrogen during cooling does not induce observable differences in graphene crystal size, suggesting that there is negligible carbon etching associated with the generation of atomic hydrogen at low partial pressures (<0.05 mbar) and temperatures <900 °C. The chamber was maintained at 3.6 mbar to reduce copper sublimation compared to LPCVD processes [63, 117], thus reducing detrimental crystallographic implications and growth kinetics complications associated with copper sublimation.

Samples were heated from below, and the precursor gases entered from the shower head manifold at the top of the reactor. Precursor and ballast gases consequently pass along a linearly ascending temperature gradient before impinging on the copper catalyst. This thermal gradient neither caused hydrogenation nor decomposition of the ethylene precursor, due to the short gas dwell time originating from the negligible flow distance (<40 mm) and low partial pressure (<0.02 mbar). The gas residence time was calculated to be  $\ll 1$  s, preventing ethylene from undergoing any significant gas-phase thermal rearrangement. Indeed, *in-situ* quadrupole mass-spectroscopy under the described growth conditions confirmed that the only carbon precursor impinging the copper surface is ethylene, while

argon, hydrogen and a trace amount of water vapor were additionally present (Figure 4.6b).

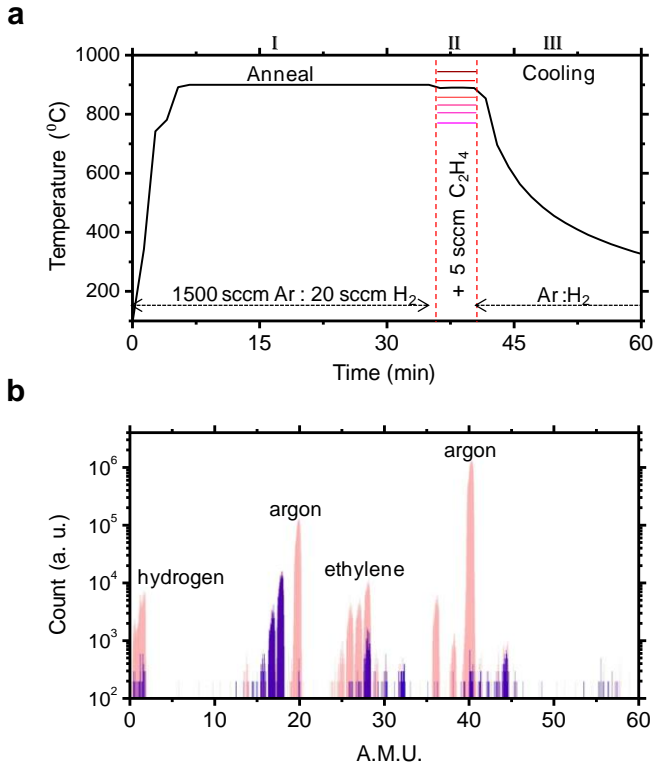


**Figure 4.6.** CVD growth conditions. (a) Details of the CVD recipe. Colored lines indicate the temperatures during the growth step. (b) *In-situ* mass spectra of the growth atmosphere during nominal growth conditions at the substrate. Purple indicates the background species which include residual water and trace amounts of nitrogen.

For Raman spectroscopic characterization, graphene films were transferred onto thermally oxidized silicon substrates (150 nm -  $\text{SiO}_2$ ) by a PMMA mediator after selective etching of the copper substrate using 10 wt% aqueous iron chloride [40, 63]. Transferred films were characterized by micro Raman spectroscopy with 457, 532 and 633

nm optical sources with incident power  $<3$  mW and a focal spot size of *ca.*  $1.2 \mu\text{m}$  (Renishaw InVia). Surface morphology was characterized using a field emission SEM (Zeiss Gemini 1530 FEG) operated at 3 kV. The mean graphene crystal sizes were extracted from measurements of *ca.* 100 crystals. Curve fitting was performed using Origin Pro 8. Crystal orientation maps were acquired by EBSD using an OIM5 system with Hikari detector (Ametek-EDAX) attached to a field emission SEM (FEI Quanta 200 FEG).

#### 4.4 Growth Kinetics

Figure 4.7 shows the representative SEM images of some graphene crystals. A clear areal enlargement is visible with increased growth time and temperature. The kinetics of this enlargement is illustrated in Figure 4.8: graphene crystal area as a function of growth time. The variation in crystal area (0.02-0.26  $\mu\text{m}^2$ ) compares well with the measured total areal ratio of graphene (Figure 4.8, inset). We rationalize our observation by a modified Gompertz function of the form [118]:

$$A(t) = A_{\max} \exp \left\{ -\exp \left[ -\frac{\mu_m e}{A_{\max}} (t - \lambda) + 1 \right] \right\}, \quad (4.1)$$

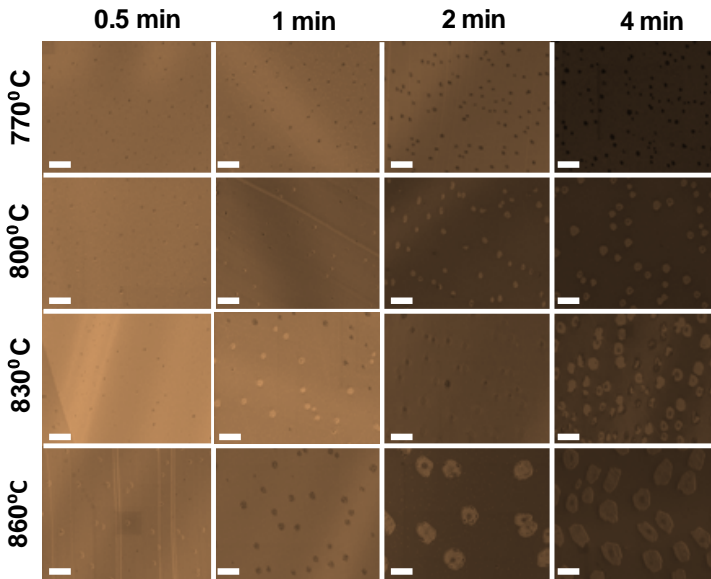


**Figure 4.7.** SEM images of the as-grown graphene crystals (round/hexagonal shaped different-contrast areas) on copper foils. The contrast difference between the crystals and copper surface originates from the oxidation of the exposed copper not protected by graphene. The darker areas at the middle of larger crystals represent secondary graphene layers.

where  $A$  is the graphene crystal area ( $\mu\text{m}^2$ ),  $A_{\text{max}}$  is the maximum area ( $\mu\text{m}^2$ ) at the growth saturation,  $\mu_m$  is the maximum growth rate ( $dA/dt$  at the inflection point),  $e$  is Euler's number,  $\lambda$  is the time lag (min) measured by the abscissa intersection of the tangent drawn from the inflection point, and  $t$  is the growth time (min). Recursive least squares ( $R^2$ ) was  $>0.97$  throughout. The present model is independent of the copper surface crystallographic orientation. The copper surface has dominant (100) symmetry after the growth independent of the growth temperature and time, as evidenced by EBSD (Figure 2.6). The initial annealing step applied to all growths was seen to define the copper lattice orientation in all cases.

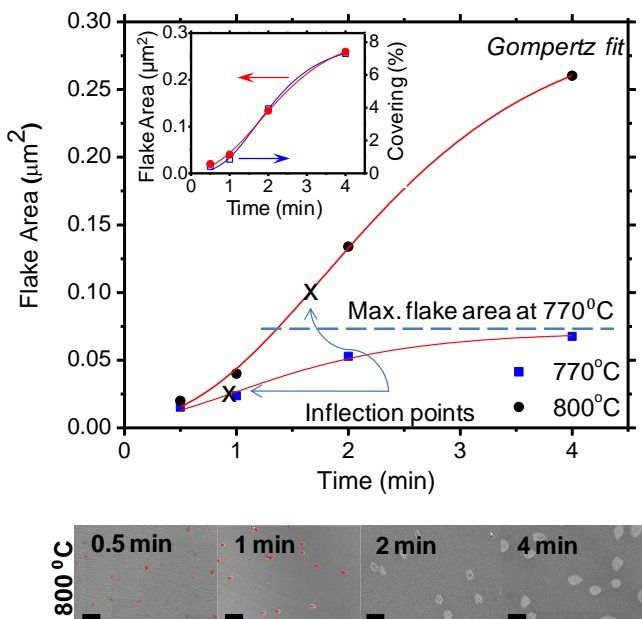


**Figure 4.8.** Analysis of the growth vs. time. Red curves indicate Gompertz fittings to the crystal size data. Inset: Comparison of the measured mean crystal size and measured percentage of the graphene area over the whole substrate surface. Bottom: Representative scanning electron micrographs show the typical crystal evolution with time, at 800 °C (Scale bar: 1  $\mu\text{m}$ ).

In order to explain the observed sigmoidal kinetic behavior we first checked if the growth duration is determined by the actual duration of hydrocarbon supply or the total duration at the growth temperature upon hydrocarbon supply. Two sets of growths were performed under the same conditions as described above, except these two parameters. When the total growth time was kept constant (2 min) and the hydrocarbon flow time was reduced (2 min flow *vs.* 1 min flow plus 1 min no-flow) the crystal size decreased, indicating that the growth is sustained by continual hydrocarbon feeding to the copper surface. However, when the hydrocarbon supply time was kept constant (1 min) and the total duration at the growth temperature was extended (1 min *vs.* 2 min, starting at the onset of the hydrocarbon flow) the crystal size did not change, additionally suggesting that the contribution of the initial supersaturated state to the growth is minimal, compared to the continual adsorption after the first nucleation phase.

Second, we consider hydrogen mediated carbon etching. If such an effect can be ruled out, then the growth can be explained simply *via* carbon reactant kinetics at the copper surface. Pre-grown samples were exposed to hydrogen partial pressures and temperatures equivalent to the growth conditions; typically, hydrogen (20 sccm) at 900 °C. No observable etching of the pre-grown graphene was found. Furthermore, growths without hydrogen showed no measurable difference in crystal size from those grown with hydrogen. Thus, we believe that the hydrogen flow rate was suitably low to obviate graphene etching. Indeed, ethylene-based graphitic carbon growth has been previously shown to be robust to changes in hydrogen partial pressure compared to other carbon feedstock [95]. Graphene etching was only notable when a significant amount (>300 sccm) of hydrogen was supplied at 1 mbar partial pressure, far away from our process window and extremely uncharacteristic for standard growth conditions.

Three main observations are critical to understand the underlying growth kinetics. First, the observed sigmoidal kinetics has an initially increasing growth rate, which again hints that a continual hydrocarbon feed is the dominant source for carbon reactants on the copper surface. If the initial supersaturation were the dominant carbon source, then the growth rate would monotonically decrease.

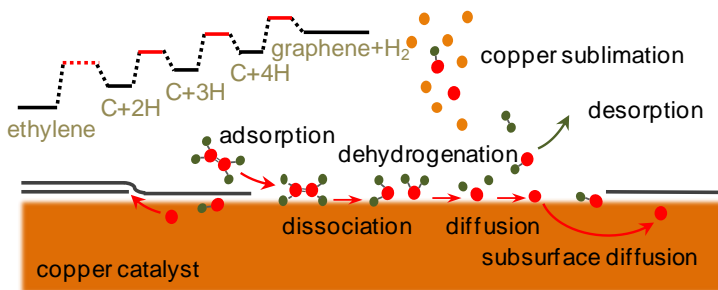


**Figure 4.9.** Growth scheme and associated mechanisms.

Thus, we conclude that the effect of the initial carbon reactant supersaturation could possibly be only critical during the nucleation phase. Second, secondary graphene nucleations take place some minutes (*ca.* 2-4 min) after the first nucleation, and the resultant secondary layers (Figure 3.9) cease growth after the first graphene layer achieves full covering. This observation also supports the continual hydrocarbon input hypothesis and indicates that these secondary graphene crystals possibly exist under the first graphene layer. The carbon reactants can diffuse beneath the first layer, as supported by previous studies [95, 119]. Lastly, the secondary graphene crystals take hexagonal shapes due to suppressed copper sublimation under the first graphene layer [117], while the first layer crystals are rather circular in shape (to be quantified later in Chapter 5). Thus, copper sublimation is an important factor for our growths.

Based on the above observations we now present a time-dependent picture of the CVD process (Figure 4.9. Growth scheme and associated mechanisms.). First, ethylene is adsorbed on the copper. Previous studies suggest that ethylene can polymerize to butadiene at 700-750 °C in the presence of copper but decompose at higher temperatures [120]. Catalytic decomposition and dehydrogenation reactions are expected for all temperatures we used. As a result, a mixture of carbon adatoms, dimers and intermediate hydrocarbon species having single or double carbon atoms could form a mixed state of reactants on the copper surface, which can undergo dissociation and dehydrogenation reactions until lattice attachment



or desorption occurs. Desorption of these reactants is enhanced on the exposed copper surface *via* the advancing copper step edges by copper sublimation. The reactants are free to diffuse around with a low energy barrier ( $<1$  eV) on the surface and subsurface of copper depending on their detailed constituents [109, 121, 122]. Carbon reactants can also diffuse beneath the graphene crystals [119], in which situation the enlarging graphene could isolate the surface reactants captured underneath it from sublimation enhanced desorption. Then, the overall amount of surface reactants can increase while the crystals continue to enlarge after the depletion of the initial carbon supersaturation.

Using the reasoning above we now construct a consistent mathematical model of the growth kinetics. The increase in the available carbon reactants density, due to the inhibited desorption/sublimation under the crystals, is presumably proportional to the prolongation of the diffusion time prior to desorption, which is in turn proportional to  $A$ . Not all the carbon reactants may be able to readily attach to the graphene lattice unless they are energetically active and sterically favorable. Cascades of catalytic dissociation and dehydrogenation reactions that these reactants go through can lead to production of the active carbon species that can readily attach to the graphene lattice [123]. This catalytic process can be much slower than the attachment reaction to the graphene lattice (will be explained later in the text); thus, reactant attachment to the graphene edge does not limit the growth kinetics (no  $\sqrt{A}$  factor present in our equation). The characteristic timescales for the variations in reactant density and surface morphology are comparable to the timescales for dissociative dehydrogenation [117]. Hence, the rate constant for the overall reaction is time-dependent, which can be best explained by the dispersive kinetics [124-126]. Taking an exponentially decaying formalism for the dispersive kinetics, it is possible to write the graphene areal enlargement rate as,

$$\frac{dA}{dt} \propto K(t)n_R \propto A \exp(-kt), \quad (4.2)$$

where  $K$  is the rate of the reaction that produces the active species that can attach to graphene,  $n_r$  is the carbon reactant density, and  $k$  represents the exponential coefficient of the time-dependent reaction rate. This proportionality is equivalent to the Gompertzian differential equation, which states

$$\frac{dA}{dt} \propto A \ln(1/A), \quad (4.3)$$

where the time-dependent exponential function in equation 4.2 is replaced by an area-dependent logarithmic function. The solution of the mechanistic expressions (eq. 4.2 and 4.3) gives eq. 4.1, which agreed well to our measured growth data. According to eq. 4.1, even for increased growth durations continuous surface covering cannot be obtained in some cases. However, if the hydrocarbon flow is increased, full covering could be achieved. Indeed, we could obtain continuous graphene by increasing the ethylene partial pressure threefold or more, as shown in Figure 3.9.

## 4.5 Thermal Behavior and Fundamental Mechanisms

Thus far we have detailed one possible explanation of the fundamental mechanisms that govern the time-dependent kinetics of graphene growth. We now focus on the thermodynamic behavior of the graphene growth by extracting information pertaining to the activation energy pathways. Figure 4.10 shows the mean crystal area as a function of growth time, and the associated Gompertz fittings at different temperatures.

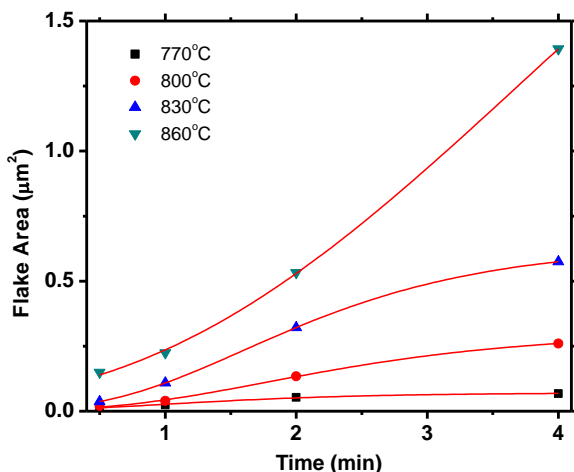


**Figure 4.10.** Graphene crystal area *vs.* growth time. Lines are the Gompertz fittings to the SEM data.

To extract the activation energy we first calculated the growth rates at each time point for different temperatures. Note that the inflection point shifts with increasing temperature, indicating that the time scales at each temperature are disparate. Using these time scales without normalization is unsuitable as the activation energy is then a measure of particular growth reactions taking place at different times at each temperature. Thus, time has been rescaled to the

characteristic time at the inflection point, thereby aligning the growth rates for each temperature according to equivalent reactions. Figure 4.11 confirms the initial increase in the growth rate attributed to the gradual increase of the graphene crystal area that isolates the reactants from the detrimental copper sublimation. The post-inflection reduction in growth rate is attributed to a reduction in the available copper surface necessary for accommodating hydrocarbon adsorption.

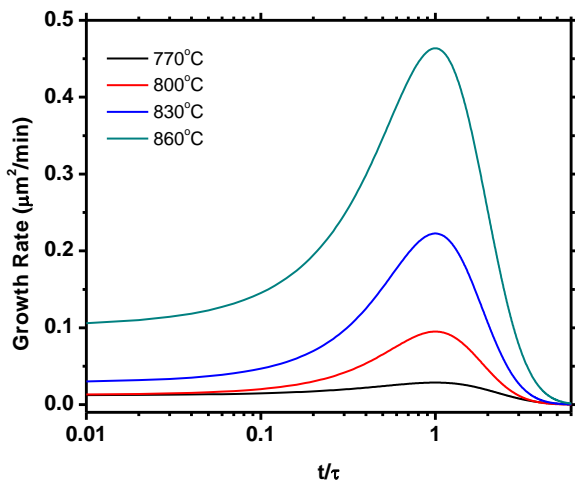


**Figure 4.11.** Growth rates vs. normalized time ( $\tau$  is the normalization factor, the time at the inflection point of the area fit for each temperature)

Activation energies were obtained as a function of normalized time (Figure 4.12). It is known that the time-dependent activation energy is associated with dispersive reaction kinetics [126]. The overall ensemble-averaged activation energy first increased from 2.4 eV to a maximum of 3.1 eV, and then it became vanishingly small when the growth saturates and stops. Here the crystal area approached an asymptotic value representing the maximum attainable crystal size at a certain supply rate of hydrocarbon feed. As a result of speeded

precursor-to-reactant catalytic conversion, the saturation area ( $A_{\text{sat}}$ ) showed an Arrhenius-type increase ( $E_A=4.2$  eV) with rising growth temperature (Figure 4.13). This strong temperature dependence and the associated thermodynamics is the subject of future study. Figure 4.13 also illustrates the time lag ( $\lambda$ ) which provides a measure of the hindrance at very early growth that affects the growth initiation and rate. In our case, copper sublimation is believed to enhance the carbon reactants desorption and impede the growth until the crystals enlarge [127]. The associated Arrhenius plot suggests a 2.7 eV barrier for this lagging effect, which is consistent with the initial activation energy of 2.4 eV.

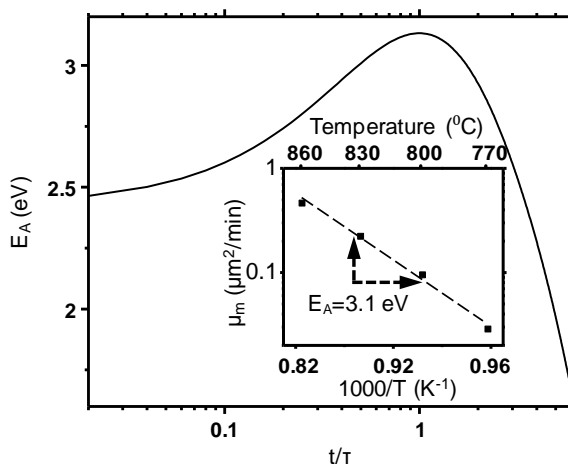


**Figure 4.12.** Time dependent activation energy ( $E_A$ ). Inset: Arrhenius plot of the inflection point growth rates

The time-dependent behavior of the activation energy raises the question of which activation energy value should be used in order to accurately define the rate-limiting reaction. The initial growth is certainly slower than the growth at the inflection point. Since a reduced growth rate may indicate an increased energy barrier, the initial activation energy may be misinterpreted to be larger than the

energy at the inflection point, which would then be a contrast with our experimental observation (2.4 eV vs. 3.1 eV). However, this could only be the case when comparing two reactions directly. Rather, the lower initial activation energy indicates a reactant-population-limited growth at the beginning of crystal enlargement, supported by making an analogy with bacterial population growth studies [128] where Gompertzian kinetics is widely applied. It is the growth rates at the inflection points that are taken into account here to calculate the activation energy independent of population dynamics occurring prior to inflection point [129]. Similarly, in the case of determining the rate-limiting step in copper-catalyzed graphene CVD, it can be inferred that the activation energy assessed from the growth rates at the inflection points would represent the best density configuration of the cascade reactions that cause the dispersive kinetics.

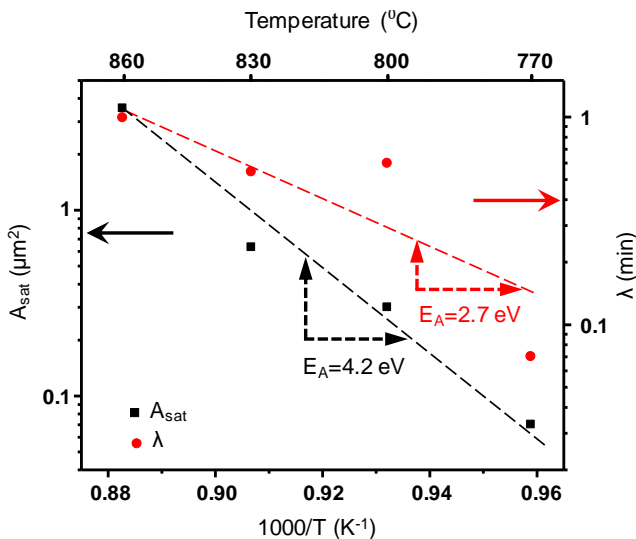


**Figure 4.13.** Arrhenius plots of the saturation area ( $A_{\text{sat}}$ , ■) and time lag ( $\lambda$ , ●).

To define the rate limiting step using the activation energy at the inflection point (3.1 eV), we account for the successive processes of;

(a) hydrocarbon adsorption on copper, (b) surface diffusion, (c) catalytic dissociation/dehydrogenation, and lastly (d) graphene lattice construction. It is very unlikely that the process is limited by atomic carbon adsorption onto the dominant surface orientations on annealed copper foils as no significant pyrolysis of ethylene was noted by *in situ* mass spectrometry (Figure 4.6b). Moreover, the energy barrier of direct carbon adatom adsorption is extremely large (4.8-6.1 eV for Cu (111) and Cu(100)) [116]. The energy barrier for hydrocarbon attachment on copper is an order of magnitude lower [95], and as such it is far from our observed activation energies. Diffusion effects can be ruled out as the energy barrier for reactant diffusion on copper is <1 eV [121, 130]. In the case of lattice attachment, the edge formation energy of graphene on copper was calculated to be 1.0 eV [97], which is also significantly smaller than our measured 3.1 eV. Lastly, the catalytic dissociative dehydrogenation of ethylene on copper can pose higher energy barriers (>2 eV) close to our activation energy [131-134]. Therefore, we propose that the rate limiting step is the dissociative dehydrogenation of ethylene on copper to produce the active carbon reactants that attach to the edge of the growing graphene lattice.

A different rate limiting step, assuming the reaction to be carbon adatom attachment, has been reported for methane-based graphene growth on copper, with an activation energy of 2.6 eV [61], where a monomolecular-like Avrami growth is observed. Such growth type is incompatible with our data. The disparity between ethylene- and methane-based growths may stem from distinct growth kinetics for each. Although this difference may be inherently physical, a strong possibility also exists that the lack of data on the very early stages in the methane-based graphene CVD reports could have limited the observation of the sigmoidal kinetics, which may have in turn prevented maximum growth rates from being obtained [135]. Indeed, in the absence of this early stage the Gompertzian kinetics may well reduce to such an Avrami growth model.

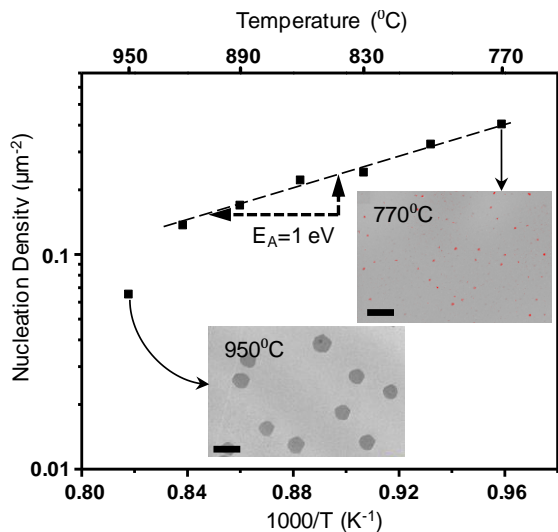


**Figure 4.14.** Arrhenius plot of the nucleation density across an extended temperature range. The Arrhenius fit with  $E_A = 1$  eV suggests an attachment-limited regime for nucleation. Deviation occurs for growth temperature  $>920$   $^{\circ}\text{C}$ . Inset(s): Typical SEM micrographs of graphene samples obtained at 770  $^{\circ}\text{C}$  and 950  $^{\circ}\text{C}$  (Scalebar: 1  $\mu\text{m}$ ).

To further discuss the differences between methane and ethylene precursors for graphene growth on copper, we have measured the areal nucleation density *vs.* temperature, including the temperatures above 900  $^{\circ}\text{C}$ . Unlike the enlarged crystals that were not sparse above 860  $^{\circ}\text{C}$ , the nucleations are sparse enough for discrete observation at even higher temperatures. Figure 4.14 shows the corresponding Arrhenius curve for the nucleation density (number of nucleation sites per unit area). A decrease in the nucleation density with respect to growth temperature is clearly seen, in agreement with previous reports [58, 61]. To explain this behavior we first rule out the initial quality effect of copper surface, as in our case the annealing condition was consistent for all growths ensuring invariant catalyst morphology and crystallinity of the copper surfaces prior to graphene nucleation. Unlike graphene lattice enlargement, the nucleation of graphene is



controlled by defect sites that initiate crystallization from an initial supersaturated state of active carbon reactants. This supersaturation is depleted in a timescale smaller than our data could resolve. If the limiting effect were the amount of the initial carbon reactants, an increase in the nucleation density would have been observed with increasing temperature. However, our experimental observations suggest otherwise that the rate increase in the carbon capture is more dominant than the increase in the rate of new nucleations, as the surface diffusion rate can also increase with temperature.

Figure 4.14 suggests a nucleation activation energy of 1 eV, with an exception above *ca.* 920 °C, where the nucleation regime is believed to change from attachment-limited to desorption-limited, due to the increased carbon removal from the copper surface at higher temperatures. A similar activation energy and high temperature deviation have also been reported for methane-based graphene CVD on copper, albeit *ca.* 50 °C lower than our result [61]. This disparity in the deviation temperature can be attributed to the lower energy barrier for catalytic dehydrogenation of ethylene on copper than methane [95].

## 4.6 Conclusions

We have presented a sigmoidal growth model to account for the graphene CVD on copper. The time and temperature dependence of crystal area and morphology suggests that the growth is driven by the continual hydrocarbon adsorption on the copper surface, rather than crystallization from an initial supersaturated pool of carbon adatoms. Copper sublimation plays an important role in inhibiting growth reactions, enhancing surface carbon desorption, thereby initially hindering growth after nucleation. When carbon reactants on the surface diffuse beneath the enlarging graphene crystals, they are sufficiently prevented from desorption and isolated from the detrimental copper sublimation. At first, this protection instigates a growth rate increase as the graphene crystals enlarge, but as the adsorption-available bare copper surface reduces in size the growth similarly reduces, saturating the crystal area. Only if the continual hydrocarbon input to the system is large can a full covering be obtained. The proportionality of growth speed with an available

amount of active carbon reactants and dispersive kinetic processes for converting simple hydrocarbon adsorbates to the active carbon reactants can be modeled by Gompertz differential model, with time-dependent activation energy. From the maximum activation energy estimation of 3.1 eV, we propose the catalytic dissociative dehydrogenation to be the rate limiting step. In conjunction with a Gompertzian growth, our analysis provides new evidence of the complex catalysis underlying that has not been hitherto proposed.



## 5 Crystal Morphology and Growth of Additional Layers

Parts of this chapter have been published in:

K. Celebi, M. T. Cole, K. B. K. Teo and H. G. Park. Observations of Early Stage Graphene Growth on Copper, *Electrochemical and Solid-State Letters*, 2012, **15**(1): K1-K4.

K. Celebi, M. T. Cole, J. W. Choi, N. Rupeshinge, F. Wyczisk, P. Legagneux, J. Robertson, K. B. K. Teo and H. G. Park. Evolutionary Kinetics of Graphene Formation on Copper, *Nano Letters*, 2013, **13**(3): pp. 967-974.

Parts of this chapter are due to be submitted for publication in *CRC Handbook of Graphene Science*.

### 5.1 Abstract

Grain morphology is critical to determination of the electronic resistance of graphene because boundary scattering of electrons by the distorted crystallinity at the boundary is the primary transport-limiting mechanism. Therefore, it is necessary to have a clear understanding of the influence of the growth on the crystal morphology. Our observation of the graphene crystal morphology establishes the effect of copper sublimation that when sublimation is suppressed the crystal morphology is dominated by the sixfold lattice symmetry, devoid of fourfold copper lattice construction. This statement is further supported by the observation of the secondary layer morphology, which is quantitatively more hexagonal than the primary layer at the top of it. In addition, the thermal behavior of the secondary layer growth is characterized, resulting in an activation energy of 2.3 eV.

## 5.2 Introduction

### *Crystal Morphology*

Graphene grown by CVD is polycrystalline. The flake crystallinity and edge morphology dramatically influence the physical and chemical properties of the as-synthesized graphene, in particular charge mobility. In this chapter we discuss the competing mechanistic models that define the crystal morphology. The morphologies reported can be defined as a mixture of dendritic and hexagonal geometries, as well as compound structures. Substrate and growth conditions intimately determine how the crystal enlargement occurs.

Wofford *et al.* have reported a real-time observation of four-lobed crystal enlargement on Cu (100) surface under ultrahigh vacuum and pure carbon precursors [117]. The growth has been claimed to be attachment-limited. As the copper sublimation cause an inhomogeneity in the copper step distribution, the crystal enlargement speed becomes orientation dependent and follows the fourfold symmetry of the underlying copper substrate (Figure 5.1a-c). However a similar study by Nie *et al.* has demonstrated for Cu (111) surface the crystal morphology changes from dendritic to hexagonal by increasing temperature [101]. Here the explanation is that the growth is diffusion-limited. Indeed, unlike the surface diffusion on Cu (100), carbon adatoms diffuse through subsurface sites on Cu (111). Subsurface diffusion may be associated with surfacing of the adatom, which may require higher energies compared to attachment. However, the surfacing mechanism is yet to be explained. At higher temperatures on Cu (111) the crystals also have lobes that follow the sixfold symmetry of the substrate due to the inhomogeneous copper step density distribution. Regarding the crystallinity, the hexagonal crystals at higher temperatures have a rather uniform crystalline orientation compared to the dendritic crystals. However, when such a crystal enlarges, passing over a copper step, the crystalline orientation may change up to  $3^\circ$ .

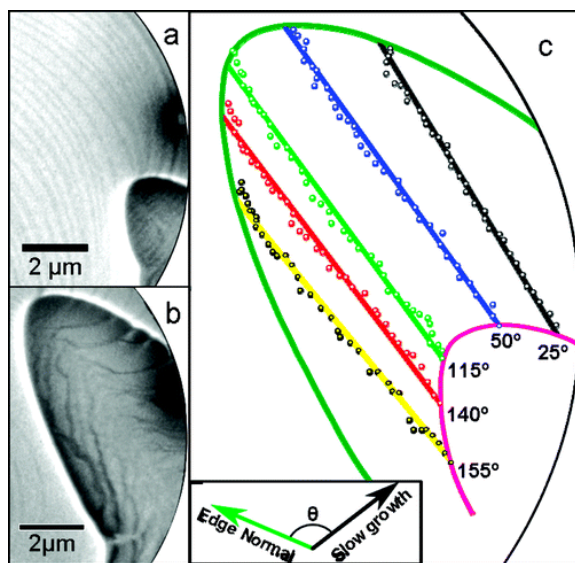


**Figure 5.1.** The LEEM image of a graphene crystal lobe at 790 °C (a), and the same lobe after 820 sec of growth (b). Time-tracks (dots) and associated linear fits (colored solid lines) of the lobe edge positions with the indicated relative angles, with respect to the slow-growth direction [117].

During the thermal dissociation of the hydrocarbon precursor atomic hydrogen is liberated. Thus, the effect of concomitant lattice etching may not be neglected during growth. Vlasiouk *et al.* have reported etching of the graphene crystal by excessive hydrogen during the growth [136]. The reported etch rate was low for the zigzag edges, thereby increasing the hexagonality of the crystal. The flake size initially benefits from the catalytic role of hydrogen, until etching becomes dominant at higher hydrogen partial pressure. However, the role of hydrogen on etching is disputed. A contrasting study by Choubak *et al.* claimed that it is the oxygen impurities in the hydrogen line that might cause the observed etching of graphene crystals [137]. Indeed, negligible etching of graphene occurred when we grew equally graphitic graphene crystals with and without a hydrogen ballast and under typical hydrogen partial pressures during growth. Nonetheless, regardless of the exact etching species, perhaps the most important finding regarding the graphene flake morphology

is that the degree of hexagonality is correlated with increasing total pressure [136, 138]. APCVD growths report hexagonal flake shapes with great crystallinity [139], although the reason for this behavior is unclear. Associated explanations include various mechanisms that occur at higher pressures, *viz*: (1) gas phase diffusion limitation [110]; (2) prevention of the copper step advancement due to the suppression of copper sublimation [67, 101]; and (3) difference in the carbon-to-crystal-edge attachment mechanism related to formation of carbon chains on the copper surface [97]. Hexagonal morphology is more favored compared with the dendritic morphology for better grain crystallinity and connectivity.

### *Secondary Layers*

CVD of graphene on copper is, under the correct growth conditions, self-terminating. That is, the growth terminates when monolayer coverage is complete. However, even for high quality monolayers, two or more additional layers often exist with covering the catalyst surface area up to a few percent of it. These layers result from secondary nucleations that occur at areas that are covered by already growing crystal. Conflicting reports exist on the nature of these nucleations. Robertson *et al.* have claim that the secondary layers exist on top of the main layer, as suggested by an atomic force microscopy [140]; however, equivalent surface profiles can also occur when these secondary nucleations are under the first layer. Furthermore, it is counterintuitive that secondary growth can be catalyzed on top of the first graphene layer. Other reports indicate the additional layers grow under the first, where the growth is still catalyzed by the copper and supported by diffusion of the carbon reactants [141, 142]. Figure 5.2a-c shows the LEEM data reported by Nie *et al.*, supporting growth from below. The intensity decrease in the secondary layer's diffraction pattern (Figure 5.2c) indicates that the second layer is below the first one. The diffraction data also shows that the underlying layer's crystalline orientation is rotated with respect to the top layer.

Various strategies can be employed to minimize the formation of the secondary layers. Han *et al.* have presented a pulsed supply scheme of the methane precursor with incubation intervals designed to allow the excess reactants to be consumed by the first layer [143]. When the

excess reactants exist, the probability of having additional nucleations under the first layer is higher. Indeed, Wassei *et al.* have revealed that increasing the carbon content in the precursor gas can promote secondary nucleations [144]. Alternatively, a carbon sink under a thin catalyst layer can also be used to limit excessive carbon content on the surface. However, this method has only been demonstrated for graphene growth on nickel thin films, with a molybdenum underlayer acting as the carbon sink material [145].

Another interesting feature of secondary nucleations is that their hexagonal morphology is more pronounced. Lobe formation is restricted under the graphene cover. This has been attributed to suppression of copper sublimation, which in turn impedes the step advancement [67]. This behavior is analogous to the APCVD studies, where the crystals are also more hexagonal with less lobes compared to LPCVD growths [97]. Such a similarity supports the sublimation-based reasoning for the determination of the crystal morphology.

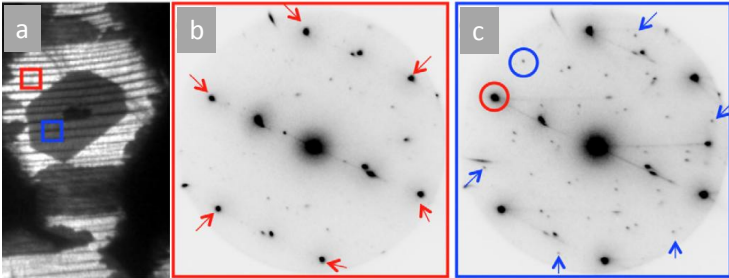


**Figure 5.2.** (a) Bright-field LEEM image of a graphene crystal (brighter hexagonal area) with secondary layer (darker hexagon in the middle). (b) Low energy electron diffraction (LEED) pattern from the area indicated by the red square in (a). (c) LEED pattern from the area indicated by the blue square in (a) [101].



## 5.3 Results and Discussion

### Crystal Morphology

While no further nucleations were observed for the main graphene layer after the near instantaneous nucleations, secondary layers of graphene emerge around the nucleation centers of the already growing graphene crystals (Figure 5.3). These secondary nucleations were only observed under larger crystals, resulting in smaller crystals enlarging and adhering to the top layer from their underside [146]. The growth of these secondary layers continued until the first monolayer completely covered the surface as the top layer prohibited further carbon intake. Figure 5.3 illustrates the temperature dependence of the secondary crystal sizes for a 4 min growth. There was no observable secondary nucleation present for shorter growth durations, especially at reduced growth temperatures. A more accurate study is ongoing. The apparent activation energy of this secondary layer growth was 2.3 eV, which is less than the activation energy of the primary layer. This result may stem from the limited number of active reactants underneath the first crystal. The first crystal can capture all the active reactants passing by, both from frontal and back sides of the extending edge in the continual influx of carbon precursor, whereas the secondary crystal can only capture active reactants that have undergone the dissociative dehydrogenation cascades underneath the associated first crystal without newly adsorbed precursor. Continued experimental and theoretical work is needed before a better understanding of such catalysis is obtained.

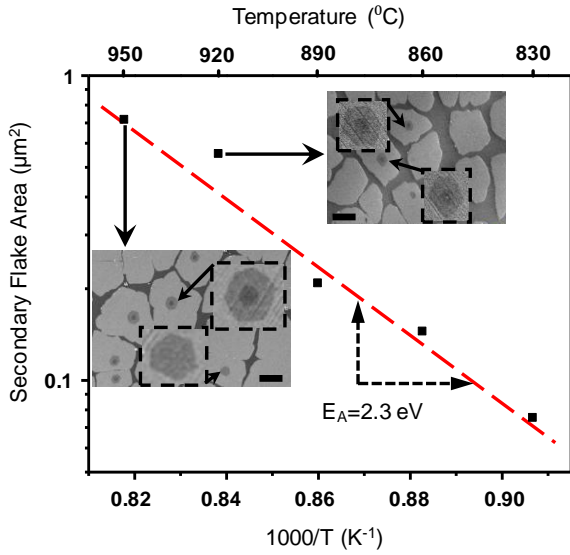


**Figure 5.3.** Arrhenius plot for secondary crystal growth. Insets: Example SEM micrographs of secondary nucleations at 950  $^{\circ}\text{C}$  and 920  $^{\circ}\text{C}$ . (Scalebar: 1  $\mu\text{m}$ )

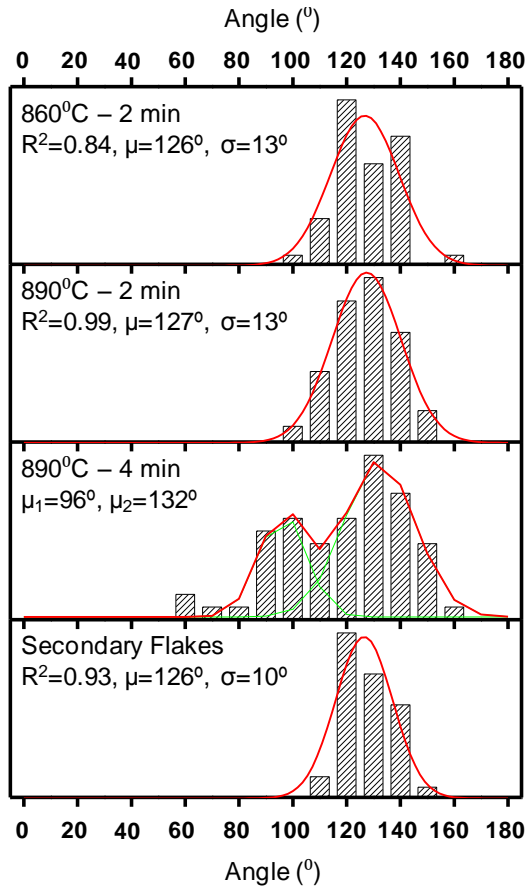


**Figure 5.4.** Time evolving distribution of the edge angles of primary and secondary crystals. Narrow single peak at  $120^\circ$  indicate strong hexagonality. Increasing temperature from  $860^\circ\text{C}$  to  $890^\circ\text{C}$  results in improved hexagonality due to the onset of stable edge formation. Further increases in time from 2 min to 4 min ( $890^\circ\text{C}$ ) results in crystal coalescence, which randomizes crystal morphology by inducing substrate-dependent preferential growth directions. Secondary crystals show narrow Gaussian distribution (red/green curves) around  $120^\circ$  ( $\sigma = 10^\circ$ ), as they are less prone to detrimental copper sublimation effects.

The effect of inhibited copper sublimation is evident from the shape of these secondary crystals. Though the associated crystals are smaller in area than the primary crystals (less than half in size), the morphologies are substantially more hexagonal in shape with a mean ( $\mu$ ) vertex angle of  $126^\circ$  and standard deviation ( $\sigma$ ) of  $10^\circ$  (Figure 5.4) compared to those of the primary crystals at the initial growth stages, supporting the postulate that reduced copper sublimation allows graphene to gain sixfold symmetry independent of the copper's fourfold symmetry [117]. In addition to the secondary crystal morphology, Figure 5.4 also shows the evolution of the primary crystal morphology. Smaller primary crystals ( $<0.5 \mu\text{m}$  in diameter) for a 2 min growth at  $860^\circ\text{C}$  tend to be more circular ( $R^2 = 0.84$ ,  $\mu = 126^\circ$ ,  $\sigma = 13^\circ$ ) indicating the less stable morphology adopted prior to the formation of stable edge fronts. As the edges become increasingly stable (*i.e.*, same growth time at higher temperature,  $890^\circ\text{C}$ ), the angle distribution forms a single Gaussian peak displaying a high degree of hexagonality ( $R^2 > 0.99$ ,  $\mu = 127^\circ$ ,  $\sigma = 13^\circ$ ) on those crystals that are large and far apart ( $>$  half of the primary crystal diameter) from one another. Following further growth ( $>2$  min), these larger crystal boundaries approach one another, coalesce and induce preferential growth directions toward the remaining unoccupied regions of the copper surface (Figure 5.5), which accounts for the shift of the angles (two distinct Gaussians evolve at  $100^\circ$  and  $130^\circ$ ). In comparison with the LPCVD-based four-lobed graphene crystals [117], hexagonality is generally more apparent in our CVD results as the total pressure was two-to-three orders of magnitude higher, thereby suppressing copper sublimation. This observation also confirms the detrimental effect of copper sublimation on the graphene crystal morphology.

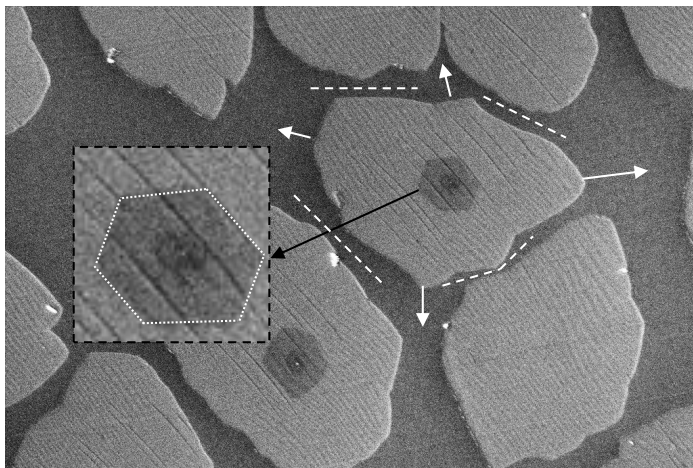


**Figure 5.5.** SEM of the large crystals from the growth at 920 °C for 4 min. The secondary graphene layer (enlarged) is free from the detrimental effect of copper and also any possible push by a nearby crystal. Thus forms the hexagonal shape as the zigzag edge is the most stable growth front. However, the main graphene crystal above cannot form the hexagonal shape even though it is large enough to be able to form the hexagonal front. This deviation from hexagonality is due to the nearby crystals preventing it to grow through the crystal boundaries (white dashed lines), thus causing preferential growth in the direction of graphene-free area (white arrows).

### *Quality and Defects*

We further characterized the crystal structure by micro Raman spatial mapping. Figure 5.6 shows areal scans for the three major Raman peaks of a transferred graphene sample (5-min growth at 850 °C). The black regions represent bare silica. The edges of the primary graphene domains are distinguished by a local increase in the *D* peak intensity that originates from the edge disorder. While most of the graphene domains show monolayer spectroscopic characteristics, some domain centers exhibit distinct variations, where the increased *D* peak indicates the edge-state defects associated with secondary nucleation. Localized layer doubling decreases the *G'* peak, but increases the *G* peak by providing more phonons. These secondary

nucleations are caused by the higher total pressure (3.1 Torr) compared to methane-based LPCVD [63, 146]. This pressure range decreases copper sublimation and causes wider and thicker copper plateaus, which in turn initiates epitaxial growth of the secondary layers around the defective nucleation centers as also recently shown by methane-based APCVD [146]. In our case, the effect of pressure is also enhanced by the increased carbon input, making our pressure range adequate to initiate secondary nucleations.

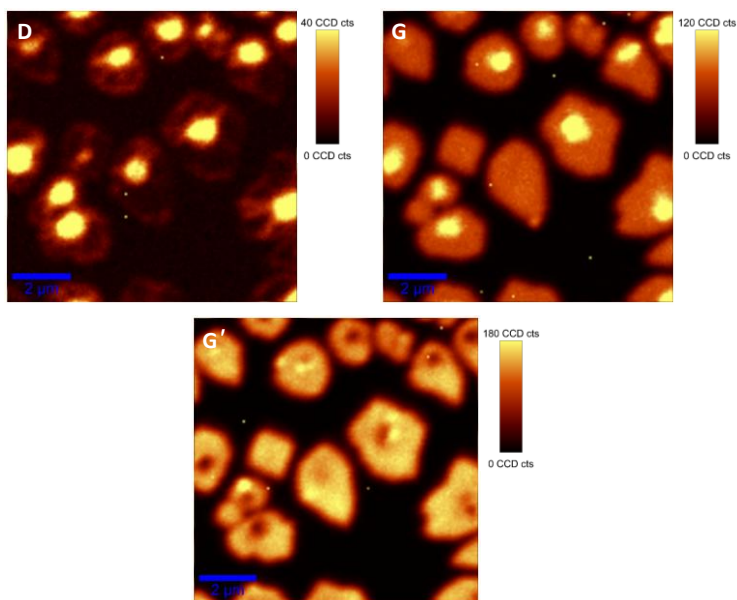


**Figure 5.6.** Two dimensional micro Raman (532 nm) spatial maps of the major Raman *D*, *G*, *G'* peaks of the transferred graphene on silica.

## 5.5 Conclusions

We have observed secondary layer nucleation underneath the initial primary graphene crystals. These nucleations start after the first layers enlarge to several-hundred nanometers in sizes. The secondary layer morphology is more hexagonal than the first layer. As the sublimation is suppressed underneath the first layer, our observation supports the claim that copper sublimation hinders the sixfold symmetry of graphene obtained. The activation energy for the secondary layer enlargement is found to be *ca.* 2.3 eV, lower than the first-layer formation activation energy. However, this value may not be the maximum energy barrier. More studies on the growth kinetics of the secondary layers are needed to solve this energy barrier mystery.





## 6 Graphene Transfer

Parts of this chapter are due to be submitted for publication in *CRC Handbook of Graphene Science*.

### 6.1 Abstract

Graphene transfer is the key to its utilization in many applications. The cleanliness in the absence of wrinkles and ripples is of great significance for obtaining high quality graphene electronically and mechanically. We have studied the transfer methods and optimized the procedures to obtain clean and mechanically robust graphene, on rigid samples and as freestanding on meshes. In this chapter we describe and compare graphene transfer procedures we have used and finally establish the clean and high-yield transfer method onto the meshes.

## 6.2 Introduction

### *Transfer Methods*

Early methods for the graphene transfer from metal substrates have proven the possibility of transferring graphene by adhesion to a sub-micrometer-thick polymer layer [147]. A common wet transfer procedure begins with spin-coating of a polymer layer, *e.g.*, PMMA, on the as-grown graphene/catalyst stack. The stack is then cured, at 180 °C for 1 min in the case of PMMA. Next, the catalyst metal is etched away, which in the case for copper is achieved using aqueous solutions of one of  $\text{FeCl}_3$  [148, 149],  $\text{Fe}(\text{NO}_3)_3$  [63],  $\text{HCl}$  [148],  $\text{HNO}_3$  [150], and  $(\text{NH}_4)_2\text{S}_2\text{O}_8$  [73, 151] at concentrations of 0.1-5 M. After the etching, the floating polymer/graphene stack is water-rinsed, fished by a destination substrate and dried. Lastly, the polymer layer is removed by a polymer etcher, *e.g.*, acetone. Improvements of this wet transfer scheme have been achieved over the past few years. For PMMA, a secondary casting process has been introduced to release the strain after the initial polymer cure [84]. Groups have also recently postponed the polymer curing from pre-copper-etching to post-drying of the destination substrate [151], which apparently encourages the PMMA/graphene to conform better to the destination dielectric substrate and so to avert the detrimental wrinkling and crack formation. Alternative fishing-out methods such as graphene picking from above, slow lowering of the liquid level, and reduced-angle pulling by a needle have also been demonstrated [151]. To retain the novel properties of the graphene it is critical to ensure cleanliness in the transfer process. As such, PMMA removal has been widely investigated for improvement, consequently reporting heated acetone [152, 153], acetone vapor [154], and additional annealing [155]. At the moment acetone is being phased out completely, being replaced by high temperature annealing, which will be discussed in detail in the following section. To exemplify the current state-of-the-art transfer [151], optimal wet-transfer trend for centimeter-sized graphene starts by the spin-coating of PMMA (2% in anisole) at *ca.* 4000 rpm, continued with copper etching by the  $(\text{NH}_4)_2\text{S}_2\text{O}_8$  solution (*ca.* 0.1-0.5 M) in two steps (first step to remove the backside graphene), followed by an air drying (*ca.* 30 min) and a vacuum drying (*ca.* 3 hours). Lastly, the PMMA layer is removed by annealing

at 400°C under argon and hydrogen (*e.g.*, 500 sccm each) for 2 hours.

Other than the common wet-transfer technique as described above, numerous wet/dry methods have been proposed [149, 156-158]. All these cases share complete removal of polymer residues as the critical issue, and a direct transfer method by exploiting the adhesion force of surface tension has been proposed to stick the as-grown graphene to TEM grids [159]. Here a drop of isopropanol is placed on a TEM grid which stays on the copper foil with graphene. While evaporating, the surface tension draws the graphene from the copper surface to the amorphous carbon grid. Because this method has low yields, PMMA-based method is still preferred by many. Alternatively, a dry transfer technique based on poly methyl-siloxane (PDMS) can be used, albeit with less conformity [149].

Large area, mass scale transfer techniques include roll-to-roll processes comprising major steps of: (1) adhering to graphene various polymers and other thermal, optical or chemical release layers; (2) etching of copper and reattaching to the desired substrate; and (3) release of the transport layers [73]. More recently, renewable procedures to avoid the copper etch step have been introduced, such as the delaminating method by Yoon *et al* [160]. Here a flexible substrate with an additional epoxy layer is adhered to the graphene. By precisely measuring the graphene-copper adhesion energy (0.72 J/m<sup>2</sup>), coupled with an appropriate choice of the epoxy/substrate pair, they removed graphene from its copper catalyst without any etching, with the aim of recycling the copper for future growths. Another alternative method to retain copper is a bubbling transfer [161, 162]. Electrochemical reduction of water generates hydrogen bubbles and detaches the graphene layer from the copper foil polarized at -5 V in a K<sub>2</sub>S<sub>2</sub>O<sub>8</sub> solution (0.05 M). However, this method still necessitates the use of a PMMA layer for mechanical integrity of the graphene layer.

### *Cleanliness*

So far no other wet or dry transfer method has surpassed the popularity of PMMA-based transfer, for almost all emerging methods

have their own distinct drawbacks as described above. The PMMA-based transfer method is the most common for research purposes using centimeter-sized graphene, due to its simplicity, high conformity, and compatibility with most of the destination substrates. However, PMMA and other polymer-based methods, often produce residues remaining on the graphene after transfer. While many organic solvents such as acetone efficiently dissolve the bulk PMMA, a thin layer (1-2 nm) often remains adsorbed. These residues could induce weak *p*-doping of the graphene [163]. A complicated wet-cleaning process based on the standard semiconductor cleaning recipes could improve residue removal [164]. Nevertheless, presently the most efficient way to clean graphene is high temperature annealing. Lin *et al.* have characterized the removal of these residues by high temperature annealing [155]. A 200 °C anneal under hydrogen removed most of the adsorbed polymer facing air, while retaining polymer (PMMA-G) and some copper particles in contact to graphene. While it is easy to remove the copper particles by replacing the common copper etchant such as FeCl<sub>3</sub> or (NH<sub>4</sub>)<sub>2</sub>S<sub>2</sub>O<sub>8</sub> [165], it is difficult to remove the PMMA-G [166]. Use of oxygen in an additional air annealing may also improve the results, through defect generation by partial graphene oxidation is a concern. Graphene annealing in hydrogen at higher temperatures such as 250 °C does not yield better cleaning, due partly to the formation of covalent bonds between PMMA and graphene that could produce *sp*<sup>3</sup> hybridization [155]. Yet, other studies report improved cleanliness at 400 °C annealing in hydrogen [151, 167]. While some processes yield transfers of CVD graphene with almost similar quality to the mechanically exfoliated graphene, better transfer and cleaning methods are yet to be developed.

## 6.3 Materials and Methods

### *Early Method*

Copper was etched away in a 1-M  $\text{FeCl}_3$  solution, and the freely floating film of graphene was fished out from the top surface of the solution by a silica/silicon substrate. This method was successful in transferring rather thick, multilayered graphene. However, as the synthesized graphene approaches to mono- or a very few layers, it becomes difficult to transfer the graphene with this method because the surface tension or the lateral flows of the thin liquid film between graphene and the pulling substrate can destabilize and tear apart the floating graphene layers. Slight reduction of surface tension through dilution of  $\text{FeCl}_3$  did not help avoiding the destabilization very much.

Thin films of PMMA then enabled the stable transfer of graphene. The PMMA (1-4% in ethyl lactate) was spun on the graphene-coated copper foil at 4000 rpm for 30 seconds, followed by a 1-min bake at 180 °C. Etch of the copper in the 1-M  $\text{FeCl}_3$  solution for one hour left the PMMA/graphene layer floating on the surface of the etchant solution. After rinsing this layer in DI water, we pulled it out with the silica/silicon substrate leaving the PMMA side facing up. Finally, removal of PMMA by acetone and isopropanol rinses exposed the graphene layer on top of the silica/silicon substrate.

### *Improved Method*

2% PMMA in anisole is first spun at 4000 rpm on copper foils, no baking is done afterwards. Then the foil has graphene on one side and PMMA/graphene on the other. These foils are etched by 0.3 M  $(\text{NH}_4)_2\text{S}_2\text{O}_8$  solution in two steps. The first 15-min step partially removes the backside graphene, which is fully removed by gently scrubbing the foil on a paper tissue after the first etch. Second etch step fully removes the copper, leaving the graphene and the fragile PMMA layer floating on the solution. This layer is then rinsed while floating by flowing DI water for 3 min, eventually replacing the etchant solution with DI water. Then the most critical step is the careful fishing-out from water with a destination substrate, followed

by 30-min-long air dry and 3-hour-long vacuum dry. Afterwards the samples are hot-plate-baked for 30 min at 180 °C, leading to PMMA curing. The last step is the PMMA removal, which is simply a 2-hour anneal in a hot furnace at 400 °C under a 500-sccm flow of hydrogen diluted by additional 500 sccm of argon. No wet process is performed after the fishing-out step. This way, the samples remain cleaner. For cleaner samples an increase in the furnace-anneal duration is helpful, but with the slight risk of damaging the graphene. Higher temperatures do not improve the cleanliness but may also damage the graphene whereas lower temperatures can be inefficient for PMMA removal.

## 6.4 Results and Discussion

### *Cleanliness*

Figure 6.1 shows an SEM image of the transferred graphene crystals (size of ca. 1  $\mu\text{m}$ ). Big PMMA chunks are visible in the figure, as indicated by the red circles. Smaller PMMA residues are also clearly visible in between the graphene crystals. The crystals, on the other hand, seem to have a thin layer of adsorbed PMMA, with associated brighter cracks or wrinkles. Figure 6.2 shows an SEM image of an improved graphene transfer, as described in the methods section. No PMMA residue can be seen, big chunks are all removed except the one indicated by the red circle in the figure. The substrate is a silicon nitride mesh and the torn-off graphene remainders can be distinguished near the pores. More details on the freestanding graphene transfer will be discussed in the next section.

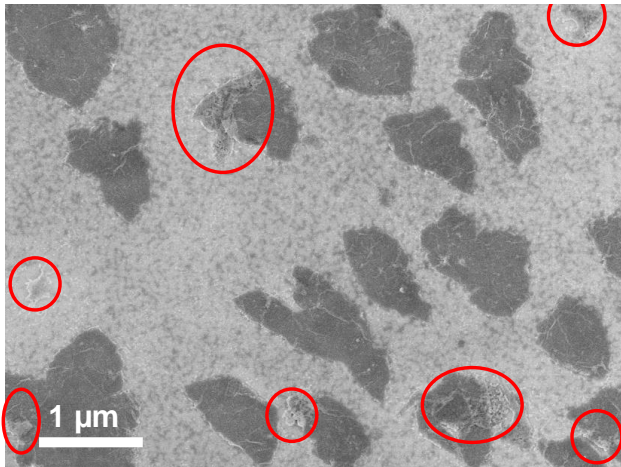


**Figure 6.1.** An SEM image of transferred graphene crystals on silica. The early method has been used for the transfer process. Red circles represent big chunks of PMMA residue.

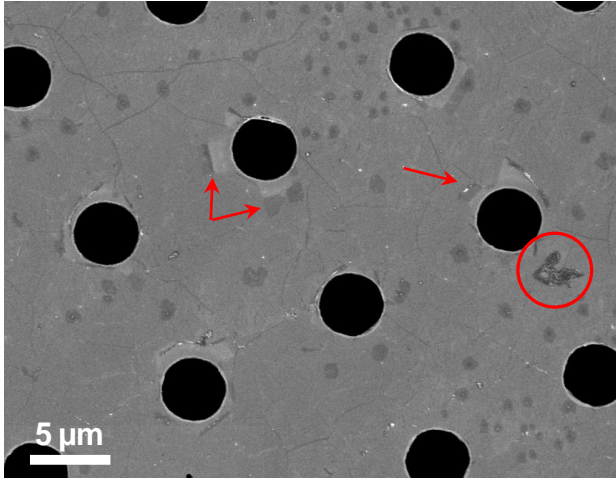


**Figure 6.2.** An SEM image of transferred graphene on a silicon nitride mesh. The improved transfer method has been used. Torn-apart graphene is visible next to some pores (indicated by arrows).

### *Transfer Yield onto Micromeshes*

We have prepared micrometer-porous meshes (micromeshes) to be able to obtain freestanding graphene membranes. However, a high quality transfer onto such substrates is more difficult than using rigid substrates. The micromeshes are based on double-side-coated low-stress silicon nitride on silicon wafers. First, photolithography is done on the backside of the wafers, to define the nitride pattern for etching through the wafer. Next, the backside etch is performed overnight in 44% KOH, yielding nitride membranes (impermeable). Then front-side photolithography and reactive ion etching are applied to perforate micrometer-sized hole-arrays on the nitride membrane. Since both photolithography steps are aligned to each other, the perforation patterns are only defined onto the freestanding nitride membrane regions (*ca.* 50-100  $\mu\text{m}$ ). Figure 6.3 shows the SEM images from the backside of the samples.



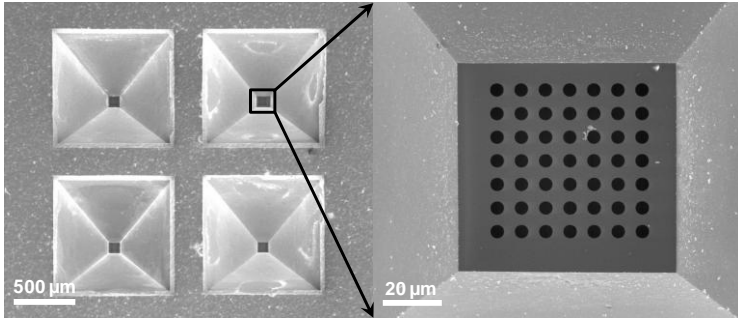


**Figure 6.3.** SEM images of the micrometer-porous silicon nitride meshes on a silicon wafer. The image has been taken from backside of the sample. The KOH-etched pits are visible on the left image. A zoomed-in image of the freestanding nitride membrane is shown in the right image.

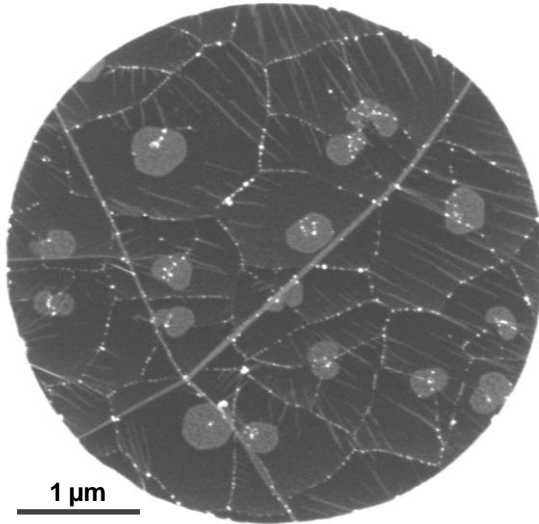


**Figure 6.4.** An SEM image of the freestanding graphene on a single nitride pore. Wrinkles (thick light-gray lines) and grain boundaries (thin light-gray lines with white dots) are visible. Lighter gray crystals are secondary layers. Small white dots originate from the sample impurities as described in Chapter 2. Parallel light-gray lines indicate intrinsic ripples.

Using the same procedure as described in the previous section, we then transfer graphene onto the micromeshes. More care is taken during the transfer, as any mistake could cause tearing of the freestanding graphene membranes. Initially we have been obtaining approximately 50% yield in the transfer, which means about half of the nitride pores uncovered by graphene. Figure 6.4 shows one successfully transferred graphene on a nitride pore. Secondary layers, wrinkles, ripples, and grain boundaries are all clearly visible in this image. The small white dots at the grain boundaries are due to the copper substrate, as explained in Chapter 2. A few dark pinholes (*ca.* 10-100 nm in diameter) are also present, possibly due to the incomplete grain connection during the growth. A 100% transfer yield has been achieved after several trials (Figure 6.5). Almost no PMMA chunks are visible and no pinholes larger than 100 nm exist.

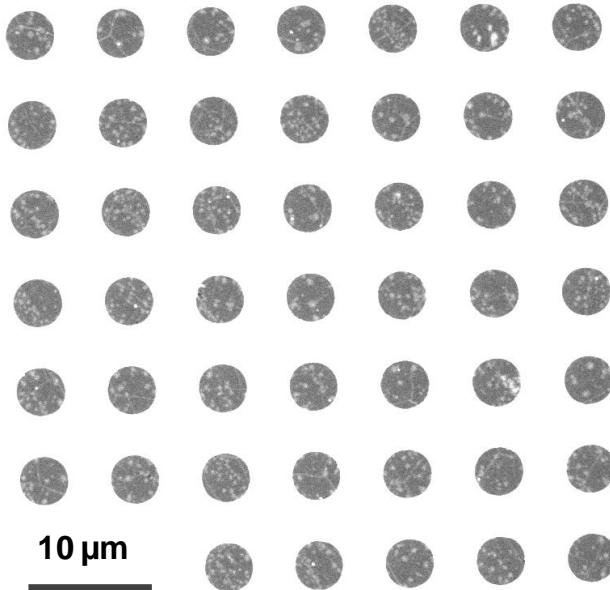


**Figure 6.5.** 100% transfer yield for freestanding graphene on micromesh. Nearby micromeshes one mm apart also have 100% yield of graphene transfer, demonstrating a millimeter-scale mechanically perfect transfer. Inset:

## **6.5 Conclusions**

An improved version of graphene transfer process with improved PMMA annealing and removal methods can provide much cleaner and mechanically stronger graphene transferred, both in freestanding and substrate-supported forms. Transfer to micromeshes can yield 100% efficient freestanding graphene transfers on a large array of micrometer-sized meshes.



## 7 Epilogue

### 7.1 Conclusions

In conclusion, the present thesis has made significant contributions toward the advancement of the process technology and the scientific understanding of the synthesis of graphene by CVD on copper. This thesis provides one of the first establishments of graphene growth on copper in Switzerland, as well as one of the first investigations on the ethylene-based CVD of graphene on copper worldwide. The present systematic study on the graphene crystal evolution has become one of the very few such reports in the literature, with the claim that the graphene growth can be mainly driven by a continual input of the carbon feedstock, rather than an initial supersaturated state.

The results presented here spans all the processing steps from the substrate preparation to the graphene transfer. The detailed conclusions can be summarized as follows:

The composition and morphology of the copper catalyst strongly influence the growth, by introducing defects, ripples and wrinkles. Careful selection and high temperature ( $>800$  °C) annealing of the copper foils are critical in order to avoid nanoparticle-originated defects and to construct graphene crystals with well-connected grains. Addition to copper of sub-100-nm metal layers, such as nickel, can be useful to reduce the growth temperature.

High quality graphene growth by ethylene precursors has been demonstrated, at lower temperatures compared to methane. The resulting continuous graphene is shown to cover over 98.4% monolayer areas, with the remaining occupied by mostly bilayer. The measured value of the electron mobility of this graphene sample is  $3,600 \text{ cm}^2\text{V}^{-1}\text{s}^{-1}$ , demonstrating good electronic grade. As evidenced by the contact angle measurements, partially covering graphene with submicron crystal sizes has been shown to modify the surface energy of the substrate due to the presence of the edge states.

The fundamental mechanism that governs the kinetics of the CVD growth of graphene is found as the catalytic dissociative dehydration

of ethylene on copper surface, with an activation energy of 3.1 eV. This finding along with the sigmoidal growth curves indicate that the crystal growth is driven by a continual feed of hydrocarbons to the surface, not by an initial carbon supersaturation.

Copper sublimation is found to hinder the growth by enhancing desorption of carbonaceous species from the surface. This hindrance is shown to influence the crystal morphology, as evidenced by the quantification of the crystal hexagonality, in particular for the secondary crystals. Secondary layers are also characterized to cause more defects near the nucleation sites.

The transfer process is critical to obtaining high electronic and mechanical quality graphene on insulating substrates. The continuous improvements in the process throughout this project have resulted in the demonstration of a 100% yield of clean, freestanding graphene on micromesh arrays at a millimeter scale.

## 7.2 Outlook

Envisioned future of graphene synthesis is threefold. Industrial-scale production of graphene is advancing fast. Meanwhile, the direct synthesis efforts on the insulating substrates are still in its infancy, and it is doubtful that this method can ever reach the popularity of the copper-based synthesis in the near future. Lastly, the scientific understanding of the graphene growth on copper is going to be critical for the future graphene industry. Therefore, the fundamental studies are becoming a popular trend in the research community. In the following these three points are discussed in brief.

### *Scaling-up Schemes*

Presently meter-scale production of graphene can only be possible by two methods: CVD growth and liquid-phase exfoliation. As excluded previously, the latter can be ruled out for most purposes because of low flake concentrations (on the order of 0.1 mg/ml) [168], very low truly monolayer flake yields (on the order of 1%) [169, 170], and most importantly the intrinsic difficulties in achieving a continuous monolayer. Hence, CVD, in particular copper-based growth, is quite possibly the only promising and viable option presently for scaling up the graphene synthesis.

Initial reports on large-scale graphene growth have been based on growths on copper foils inside large-diameter tube furnaces, with foils up to 20 cm having been demonstrated coupled with roll-to-roll transfer processes for coating plastic substrates [73]. Later, a small roll-to-roll system has been fitted into a 25-mm-diameter quartz tube by Hesjedal, to produce low quality graphene on a narrow but continuous copper foil [171]. Yamada *et al.* have employed a more advanced rolling system in a microwave plasma oven, to obtain defective graphene (at a width of 294 mm) at temperatures below 400 °C with rather high sheet resistances of 10-700 k $\Omega$ /□ that is perhaps well-suited for the flexible transparent conductor applications [172]. An increasingly advanced roll-to-roll system was reported by Kobayashi *et al* [60], where a 100-meter-long sheet of graphene, with a charge mobility of 900 cm<sup>2</sup>V<sup>-1</sup>s<sup>-1</sup>, has been grown and transferred onto flexible plastic substrates by a series of roll-to-roll processes.

Meanwhile, Tao *et al.* have demonstrated better quality graphene, uniform over a 150 mm wafer, with Raman  $G'$  peak widths of 25-35  $\text{cm}^{-1}$  and a charge mobility of 4,900  $\text{cm}^2\text{V}^{-1}\text{s}^{-1}$  [71]. They employed copper thin film on a silica/silicon wafers which restricted the rolling process but enhanced the material quality [70] similar to what we obtained in this project. Work is still ongoing throughout the industry to improve the quality and scalability of roll-to-roll and large-scale wafer-based CVD growth schemes.

### *Direct Synthesis on Insulating Substrates*

While CVD-based synthesis of graphene on copper is today's standard method to obtain scalable graphene, it has intrinsic problems such as the introduction of wrinkles and ripples due to thermal mismatch and copper surface morphology. Although the end product on an insulating substrate can have performance comparable to the mechanically exfoliated counterparts, direct synthesis of graphene on insulating substrates is the ultimate solution to avoid transfer and the associated problems.

Several studies have demonstrated graphene-like film deposition on thermal silicon oxides [173-175], quartz [74], sapphire [176-178], boron nitride [179], mica [180], and MgO [181]. Early work by Ismach *et al.* has shown that growth on thin film copper on quartz, followed by the sublimation of the copper layer, left the graphene on the quartz substrate [74]. However, the continuity and the quality of the resulting graphene were low with particular regard to film wrinkling. Alternatively, thin film copper or nickel can be used on insulating substrates as a layer to diffuse and catalyze carbon reactants to form graphene at the substrate-catalyst interface [173, 174]. Su *et al.* have reported a moderate charge mobility of 670  $\text{cm}^2\text{V}^{-1}\text{s}^{-1}$  based on diffusion through copper thin films on thermal silica [173]. This method is promising, yet still requires a metal removal step after the growth. To avoid this etch step a remote catalysis method has been demonstrated [104]. Methane is first flown over a copper foil placed upstream in a tube furnace, which catalyzes methane dissociation at 1000 °C. Next, the active carbon species are desorbed from the copper surface along with the subliming copper. These species then deposit



onto the destination substrate while flowing downstream where graphene is grown, yielding mobility values of 100-600  $\text{cm}^2\text{V}^{-1}\text{s}^{-1}$ .

The most promising form of graphene synthesis on insulators is a metal-free growth. Hwang *et al.* in 2010 demonstrated a propane-based CVD of graphene on sapphire (0001) at temperatures above 1350 °C [177]. Later a lower temperature growth was achieved by employing alcohol as the carbon source, albeit giving inferior electronic quality [178]. More recently, a high charge mobility of 3,000  $\text{cm}^2\text{V}^{-1}\text{s}^{-1}$  has been obtained by Fanton *et al.* using a methane-based CVD on sapphire at 1550 °C [176]. High growth temperatures could be a drawback, for they limit the range of available substrate materials. Molecular beam epitaxy from pure carbon filaments can be used on biotite mica (001) surfaces, heated to 500-1000 °C [180]. Furthermore, MgO-based substrates can yield growth at even lower temperatures of 325 °C using acetylene [181].

With limited choice of substrate and temperature, direct CVD on insulators remains to be much improved before produced graphene reaching quality comparable to Cu-based CVD methods.

### *Fundamental Studies*

While meter-scale graphene growth has been demonstrated experimentally, a good fundamental understanding of the graphene growth is crucial to the quality optimization and the cost reduction in the future graphene manufacturing industry. The studies on the fundamental understanding of the graphene growth on copper are limited to a few reports. To understand and optimize the growth, more studies are necessary. In particular the understanding of the growth kinetics for different pressure and flow regimes is yet to be developed. Compared to the first layer growth, the secondary layer kinetics and nucleation mechanisms are even less known. Furthermore, the studies on the formation mechanism and artificial control of wrinkles and ripples are quite important to obtaining electronic grade graphene, and yet the literature on this subject is also very limited.



## Bibliography

- [1] Novoselov KS, Geim AK, Morozov SV, Jiang D, Zhang Y, Dubonos SV, Grigorieva IV, Firsov AA. Electric Field Effect in Atomically Thin Carbon Films. *Science* 2004;306:666-9.
- [2] Bolotin KI, Sikes KJ, Jiang Z, Klima M, Fudenberg G, Hone J, Kim P, Stormer HL. Ultrahigh electron mobility in suspended graphene. *Solid State Commun* 2008;146:351-5.
- [3] Du X, Skachko I, Barker A, Andrei EY. Approaching ballistic transport in suspended graphene. *Nat Nanotechnol* 2008;3:491-5.
- [4] Morozov S, Novoselov K, Katsnelson M, Schedin F, Elias D, Jaszczak J, Geim A. Giant intrinsic carrier mobilities in graphene and its bilayer. *Phys Rev Lett* 2008;100:016602.
- [5] Geim AK, Novoselov KS. The rise of graphene. *Nat Materials* 2007;6:183-91.
- [6] Neto AC, Guinea F, Peres N, Novoselov K, Geim A. The electronic properties of graphene. *Rev Mod Phys* 2009;81:109.
- [7] Wallace PR. The band theory of graphite. *Phys Rev* 1947;71:622-34.
- [8] Bao Q, Zhang H, Wang Y, Ni Z, Yan Y, Shen ZX, Loh KP, Tang DY. Atomic-Layer Graphene as a Saturable Absorber for Ultrafast Pulsed Lasers. *Adv Funct Mater* 2009;19:3077-83.
- [9] Bonaccorso F, Sun Z, Hasan T, Ferrari A. Graphene photonics and optoelectronics. *Nat Photonics* 2010;4:611-22.
- [10] Bunch JS, van der Zande AM, Verbridge SS, Frank IW, Tanenbaum DM, Parpia JM, Craighead HG, McEuen PL. Electromechanical Resonators from Graphene Sheets. *Science* 2007;315:490-3.
- [11] Balandin AA, Ghosh S, Bao W, Calizo I, Teweldebrhan D, Miao F, Lau CN. Superior Thermal Conductivity of Single-Layer Graphene. *Nano Lett* 2008;8:902-7.
- [12] Becerril HA, Mao J, Liu Z, Stoltenberg RM, Bao Z, Chen Y. Evaluation of solution-processed reduced graphene oxide films as transparent conductors. *ACS Nano* 2008;2:463-70.
- [13] Wassei JK, Kaner RB. Graphene, a promising transparent conductor. *Mat Today* 2010;13:52-9.
- [14] Areshkin DA, White CT. Building Blocks for Integrated Graphene Circuits. *Nano Lett* 2007;7:3253-9.
- [15] Lin Y-M, Dimitrakopoulos C, Jenkins KA, Farmer DB, Chiu H-Y, Grill A, Avouris P. 100-GHz Transistors from Wafer-Scale Epitaxial Graphene. *Science* 2010;327:662.

- [16] Lin Y-M, Jenkins KA, Valdes-Garcia A, Small JP, Farmer DB, Avouris P. Operation of Graphene Transistors at Gigahertz Frequencies. *Nano Lett* 2008;9:422-6.
- [17] Moon J, Curtis D, Hu M, Wong D, McGuire C, Campbell P, Jernigan G, Tedesco J, VanMil B, Myers-Ward R. Epitaxial-graphene RF field-effect transistors on Si-face 6H-SiC substrates. *Electron Device Letters, IEEE* 2009;30:650-2.
- [18] Stoller MD, Park S, Zhu Y, An J, Ruoff RS. Graphene-based ultracapacitors. *Nano Lett* 2008;8:3498-502.
- [19] Wang C, Li D, Too CO, Wallace GG. Electrochemical Properties of Graphene Paper Electrodes Used in Lithium Batteries. *Chem Mater* 2009;21:2604-6.
- [20] Xiao J, Mei D, Li X, Xu W, Wang D, Graff GL, Bennett WD, Nie Z, Saraf LV, Aksay IA, Liu J, Zhang J-G. Hierarchically Porous Graphene as a Lithium-Air Battery Electrode. *Nano Lett* 2011;11:5071-8.
- [21] Suk ME, Aluru NR. Water Transport through Ultrathin Graphene. *J Phys Chem Lett* 2010;1:1590-4.
- [22] Chen S, Brown L, Levendorf M, Cai W, Ju S-Y, Edgeworth J, Li X, Magnuson CW, Velamakanni A, Piner RD. Oxidation resistance of graphene-coated Cu and Cu/Ni alloy. *ACS Nano* 2011;5:1321-7.
- [23] Sutter E, Albrecht P, Camino FE, Sutter P. Monolayer graphene as ultimate chemical passivation layer for arbitrarily shaped metal surfaces. *Carbon* 2010;48:4414-20.
- [24] Stankovich S, Dikin DA, Dommett GH, Kohlhaas KM, Zimney EJ, Stach EA, Piner RD, Nguyen ST, Ruoff RS. Graphene-based composite materials. *Nature* 2006;442:282-6.
- [25] Hernandez Y, Nicolosi V, Lotya M, Blighe FM, Sun Z, De S, McGovern IT, Holland B, Byrne M, Gun'Ko YK, Boland JJ, Niraj P, Duesberg G, Krishnamurthy S, Goodhue R, Hutchison J, Scardaci V, Ferrari AC, Coleman JN. High-yield production of graphene by liquid-phase exfoliation of graphite. *Nat Nano* 2008;3:563-8.
- [26] Eda G, Fanchini G, Chhowalla M. Large-area ultrathin films of reduced graphene oxide as a transparent and flexible electronic material. *Nat Nano* 2008;3:270-4.
- [27] Berger C, Song Z, Li X, Wu X, Brown N, Naud C, Mayou D, Li T, Hass J, Marchenkov AN, Conrad EH, First PN, de Heer WA. Electronic Confinement and Coherence in Patterned Epitaxial Graphene. *Science* 2006;312:1191-6.
- [28] De Heer WA, Berger C, Wu X, First PN, Conrad EH, Li X, Li T, Sprinkle M, Hass J, Sadowski ML. Epitaxial graphene. *Solid State Commun* 2007;143:92-100.
- [29] Emtsev KV, Bostwick A, Horn K, Jobst J, Kellogg GL, Ley L, McChesney JL, Ohta T, Reshanov SA, Rohrl J, Rotenberg E, Schmid AK, Waldmann D, Weber HB, Seyller T. Towards wafer-size graphene

- layers by atmospheric pressure graphitization of silicon carbide. *Nature Materials* 2009;8:203-7.
- [30] Lin Y-M, Valdes-Garcia A, Han S-J, Farmer DB, Meric I, Sun Y, Wu Y, Dimitrakopoulos C, Grill A, Avouris P. Wafer-scale graphene integrated circuit. *Science* 2011;332:1294-7.
- [31] Cai J, Ruffieux P, Jaafar R, Bieri M, Braun T, Blankenburg S, Muoth M, Seitsonen AP, Saleh M, Feng X. Atomically precise bottom-up fabrication of graphene nanoribbons. *Nature* 2010;466:470-3.
- [32] Morgan AE, Somorjai GA. Low energy electron diffraction studies of gas adsorption on the platinum (100) single crystal surface. *Surf Sci* 1968;12:405-25.
- [33] Blakely J, Kim J, Potter H. Segregation of Carbon to the (100) Surface of Nickel. *J Appl Phys* 1970;41:2693-7.
- [34] May JW. Platinum surface LEED rings. *Surf Sci* 1969;17:267-70.
- [35] Landau L. Zur Theorie der Phasenumwandlungen II. *Phys Z Sowjetunion* 1937;11:26-35.
- [36] Mermin ND. Crystalline order in two dimensions. *Phys Rev* 1968;176:250.
- [37] Peierls RE. Quelques propriétés typiques des corps solides. *Ann I H Poincaré* 1935;5:177-222.
- [38] Somani PR, Somani SP, Umeno M. Planar nano-graphenes from camphor by CVD. *Chem Phys Lett* 2006;430:56-9.
- [39] Kim KS, Zhao Y, Jang H, Lee SY, Kim JM, Kim KS, Ahn J-H, Kim P, Choi J-Y, Hong BH. Large-scale pattern growth of graphene films for stretchable transparent electrodes. *Nature* 2009;457:706-10.
- [40] Reina A, Jia X, Ho J, Nezich D, Son H, Bulovic V, Dresselhaus M, Kong J. Large area, few-layer graphene films on arbitrary substrates by chemical vapor deposition. *Nano Letters* 2009;9:30-5.
- [41] Kondo D, Sato S, Yagi K, Harada N, Sato M, Nihei M, Yokoyama N. Low-Temperature Synthesis of Graphene and Fabrication of Top-Gated Field Effect Transistors without Using Transfer Processes. *Appl Phys Expr* 2010;3:5102.
- [42] Oznuluer T, Pince E, Polat EO, Balci O, Salihoglu O, Kocabas C. Synthesis of graphene on gold. *Appl Phys Lett* 2011;98:183101-3.
- [43] John R, Ashokreddy A, Vijayan C, Pradeep T. Single- and few-layer graphene growth on stainless steel substrates by direct thermal chemical vapor deposition. *Nanotechnology* 2011;22:165701.
- [44] Loginova E, Bartelt NC, Feibelman PJ, McCarty KF. Evidence for graphene growth by C cluster attachment. *New J Phys* 2008;10:093026.
- [45] Sutter PW, Flege J-I, Sutter EA. Epitaxial graphene on ruthenium. *Nature Materials* 2008;7:406-11.

- [46] Coraux J, N'Diaye T, Engler M, Busse C, Wall D, Buckanie N, zu Heringdorf FJM, van Gaste R, Poelsema B, Michely T. Growth of graphene on Ir (111). *New J Phys* 2009;11:023006.
- [47] van Gestel R, N'Diaye AT, Wall D, Coraux J, Busse C, Buckanie NM, Heringdorf FJMz, von Hoegen MH, Michely T, Poelsema B. Selecting a single orientation for millimeter sized graphene sheets. *Appl Phys Lett* 2009;95:121901-3.
- [48] Wang B, Caffio M, Bromley C, Früchtl H, Schaub R. Coupling Epitaxy, Chemical Bonding, and Work Function at the Local Scale in Transition Metal-Supported Graphene. *ACS Nano* 2010;4:5773-82.
- [49] Fujita T, Kobayashi W, Oshima C. Novel structures of carbon layers on a Pt(111) surface. *Surf Interface Anal* 2005;37:120-3.
- [50] Land TA, Michely T, Behm RJ, Hemminger JC, Comsa G. STM investigation of single layer graphite structures produced on Pt(111) by hydrocarbon decomposition. *Surf Sci* 1992;264:261-70.
- [51] Kwon S-Y, Ciobanu CV, Petrova V, Shenoy VB, Bareño J, Gambin V, Petrov I, Kodambaka S. Growth of Semiconducting Graphene on Palladium. *Nano Lett* 2009;9:3985-90.
- [52] Weatherup RS, Bayer BC, Blume R, Ducati C, Baetz C, Schlögl R, Hofmann S. In situ characterization of alloy catalysts for low-temperature graphene growth. *Nano Lett* 2011;11:4154-60.
- [53] Lin T, Huang FQ, Wan D, Bi H, Xie X, Jiang M. Self-regulating homogenous growth of high-quality graphene on Co-Cu composite substrate for layer control. *Nanoscale* 2013.
- [54] Liu N, Fu L, Dai B, Yan K, Liu X, Zhao R, Zhang Y, Liu Z. Universal Segregation Growth Approach to Wafer-Size Graphene from Non-Noble Metals. *Nano Lett* 2010;11:297-303.
- [55] Liao Q, Zhang H, Wu K, Li H, Bao S, He P. Nucleation and growth of monodispersed cobalt nanoclusters on graphene moire on Ru (0001). *Nanotechnology* 2011;22:125303.
- [56] N'Diaye AT, Bleikamp S, Feibelman PJ, Michely T. Two-dimensional Ir cluster lattice on a graphene moire on Ir (111). *Phys Rev Lett* 2006;97:215501.
- [57] Mattevi C, Kim H, Chhowalla M. A review of chemical vapour deposition of graphene on copper. *J Mater Chem* 2011;21:3324-34.
- [58] Li X, Magnuson CW, Venugopal A, An J, Suk JW, Han B, Borysiak M, Cai W, Velamakanni A, Zhu Y, Fu L, Vogel EM, Voelkl E, Colombo L, Ruoff RS. Graphene Films with Large Domain Size by a Two-Step Chemical Vapor Deposition Process. *Nano Lett* 2010;10:4328-34.
- [59] Tsen AW, Brown L, Levendorf MP, Ghahari F, Huang PY, Havener RW, Ruiz-Vargas CS, Muller DA, Kim P, Park J. Tailoring Electrical Transport Across Grain Boundaries in Polycrystalline Graphene. *Science* 2012;336:1143-6.

- [60] Kobayashi T, Bando M, Kimura N, Shimizu K, Kadono K, Umezu N, Miyahara K, Hayazaki S, Nagai S, Mizuguchi Y, Murakami Y, Hobara D. Production of a 100-m-long high-quality graphene transparent conductive film by roll-to-roll chemical vapor deposition and transfer process. *Applied Physics Letters* 2013;102:023112-4.
- [61] Kim H, Mattevi C, Calvo MR, Oberg JC, Artiglia L, Agnoli S, Hirjibehedin CF, Chhowalla M, Saiz E. Activation Energy Paths for Graphene Nucleation and Growth on Cu. *ACS Nano* 2012;6:3614-23.
- [62] Hansen M, Shunk FA, Elliott RP, Anderko K. Constitution of binary alloys: McGraw-Hill New York; 1965.
- [63] Yao Y, Feng C, Zhang J, Liu Z. "Cloning" of Single-Walled Carbon Nanotubes via Open-End Growth Mechanism. *Nano Lett* 2009;9:1673-7.
- [64] Zhang B, Lee WH, Piner R, Kholmanov I, Wu Y, Li H, Ji H, Ruoff RS. Low-Temperature Chemical Vapor Deposition Growth of Graphene from Toluene on Electropolished Copper Foils. *ACS Nano* 2012;6:2471-6.
- [65] Han GH, Güneş F, Bae JJ, Kim ES, Chae SJ, Shin H-J, Choi J-Y, Pribat D, Lee YH. Influence of Copper Morphology in Forming Nucleation Seeds for Graphene Growth. *Nano Lett* 2011;11:4144-8.
- [66] Levendorf MP, Ruiz-Vargas CS, Garg S, Park J. Transfer-Free Batch Fabrication of Single Layer Graphene Transistors. *Nano Lett* 2009;9:4479-83.
- [67] Celebi K, Cole MT, Choi JW, Wyczisk F, Legagneux P, Rupesinghe N, Robertson J, Teo KBK, Park HG. Evolutionary Kinetics of Graphene Formation on Copper. *Nano Lett* 2013;13:967-74.
- [68] Wood JD, Schmucker SW, Lyons AS, Pop E, Lyding JW. Effects of Polycrystalline Cu Substrate on Graphene Growth by Chemical Vapor Deposition. *Nano Lett* 2011;11:4547-54.
- [69] Gao L, Guest JR, Guisinger NP. Epitaxial Graphene on Cu(111). *Nano Lett* 2010;10:3512-6.
- [70] Tao L, Lee J, Chou H, Holt M, Ruoff RS, Akinwande D. Synthesis of High Quality Monolayer Graphene at Reduced Temperature on Hydrogen-Enriched Evaporated Copper (111) Films. *ACS Nano* 2012;6:2319-25.
- [71] Tao L, Lee J, Holt M, Chou H, McDonnell SJ, Ferrer DA, Babenco MG, Wallace RM, Banerjee SK, Ruoff RS, Akinwande D. Uniform Wafer-Scale Chemical Vapor Deposition of Graphene on Evaporated Cu (111) Film with Quality Comparable to Exfoliated Monolayer. *J Phys Chem C* 2012;116:24068-74.
- [72] Kidambi PR, Ducati C, Dlubak B, Gardiner D, Weatherup RS, Martin M-B, Seneor P, Coles H, Hofmann S. The Parameter Space of Graphene Chemical Vapor Deposition on Polycrystalline Cu. *J Phys Chem C* 2012;116:22492-501.

- [73] Bae S, Kim H, Lee Y, Xu X, Park J-S, Zheng Y, Balakrishnan J, Lei T, Ri Kim H, Song YI, Kim Y-J, Kim KS, Ozyilmaz B, Ahn J-H, Hong BH, Iijima S. Roll-to-roll production of 30-inch graphene films for transparent electrodes. *Nat Nano* 2010;5:574-8.
- [74] Ismach A, Druzgalski C, Penwell S, Schwartzberg A, Zheng M, Javey A, Bokor J, Zhang Y. Direct Chemical Vapor Deposition of Graphene on Dielectric Surfaces. *Nano Lett* 2010;10:1542-8.
- [75] Verma VP, Das S, Lahiri I, Choi W. Large-area graphene on polymer film for flexible and transparent anode in field emission device. *Appl Phys Lett* 2010;96:203108-3.
- [76] Jung M, Yong Eun K, Lee J-K, Baik Y-J, Lee K-R, Wan Park J. Growth of carbon nanotubes by chemical vapor deposition. *Diamond and Related Materials* 2001;10:1235-40.
- [77] Lee Y-H, Lee J-H. Scalable growth of free-standing graphene wafers with copper(Cu) catalyst on SiO<sub>2</sub>/Si substrate: Thermal conductivity of the wafers. *Appl Phys Lett* 2010;96:083101-3.
- [78] Xu Y-Q, Flor E, Schmidt H, Smalley RE, Hauge RH. Effects of atomic hydrogen and active carbon species in 1 mm vertically aligned single-walled carbon nanotube growth. *Applied Physics Letters* 2006;89:123116-3.
- [79] Okita A, Suda Y, Oda A, Nakamura J, Ozeki A, Bhattacharyya K, Sugawara H, Sakai Y. Effects of hydrogen on carbon nanotube formation in CH<sub>4</sub>/H<sub>2</sub> plasmas. *Carbon* 2007;45:1518-26.
- [80] Zhang G, Mann D, Zhang L, Javey A, Li Y, Yenilmez E, Wang Q, McVittie JP, Nishi Y, Gibbons J, Dai H. Ultra-high-yield growth of vertical single-walled carbon nanotubes: Hidden roles of hydrogen and oxygen. *PNAS* 2005;102:16141-5.
- [81] Ferrari AC, Meyer JC, Scardaci V, Casiraghi C, Lazzeri M, Mauri F, Piscanec S, Jiang D, Novoselov KS, Roth S, Geim AK. Raman Spectrum of Graphene and Graphene Layers. *Phys Rev Lett* 2006;97:187401.
- [82] Li X, Cai W, Colombo L, Ruoff R. Evolution of graphene growth on Cu and Ni studied by carbon isotope labeling. *Nano Letters* 2009;9:4268-72.
- [83] Malard LM, Pimenta MA, Dresselhaus G, Dresselhaus MS. Raman spectroscopy in graphene. *Phys Rep* 2009;473:51-87.
- [84] Li X, Zhu Y, Cai W, Borysiak M, Han B, Chen D, Piner RD, Colombo L, Ruoff RS. Transfer of Large-Area Graphene Films for High-Performance Transparent Conductive Electrodes. *Nano Lett* 2009;9:4359-63.
- [85] Hass J, Varchon F, Millán-Otoya JE, Sprinkle M, Sharma N, de Heer WA, Berger C, First PN, Magaud L, Conrad EH. Why Multilayer Graphene on 4H-SiC(0001-bar) Behaves Like a Single Sheet of Graphene. *Physical Review Letters* 2008;100:125504.



- [86] Matthews MJ, Pimenta MA, Dresselhaus G, Dresselhaus MS, Endo M. Origin of dispersive effects of the Raman D band in carbon materials. *Phys Rev B* 1999;59:R6585.
- [87] Wang X, Dai H. Etching and narrowing of graphene from the edges. *Nat Chem* 2010;2:661-5.
- [88] Gao L, Guest JR, Guisinger NP. Epitaxial Graphene on Cu(111). *Nano Lett* 2010:Article ASAP.
- [89] Leenaerts O, Partoens B, Peeters FM. Water on graphene: Hydrophobicity and dipole moment using density functional theory. *Physical Review B* 2009;79:235440.
- [90] Gordillo MC, Martí J. Effect of Surface Roughness on the Static and Dynamic Properties of Water Adsorbed on Graphene. *The Journal of Physical Chemistry B* 2010;114:4583-9.
- [91] Cicero G, Grossman JC, Schwegler E, Gygi F, Galli G. Water Confined in Nanotubes and between Graphene Sheets: A First Principle Study. *Journal of the American Chemical Society* 2008;130:1871-8.
- [92] Markovic N, Andersson PU, Någård MB, Pettersson JBC. Scattering of water from graphite: simulations and experiments. *Chemical Physics* 1999;247:413-30.
- [93] Werder T, Walther JH, Jaffe RL, Halicioglu T, Koumoutsakos P. On the Water-Carbon Interaction for Use in Molecular Dynamics Simulations of Graphite and Carbon Nanotubes. *J Phys Chem B* 2003;107:1345-52.
- [94] Hummer G, Rasaiah JC, Noworyta JP. Water conduction through the hydrophobic channel of a carbon nanotube. *Nature* 2001;414:188-90.
- [95] Zhang W, Wu P, Li Z, Yang J. First-Principles Thermodynamics of Graphene Growth on Cu Surfaces. *J Phys Chem C* 2011;115:17782-7.
- [96] Jia C, Jiang J, Gan L, Guo X. Direct Optical Characterization of Graphene Growth and Domains on Growth Substrates. *Sci Rep* 2012;2.
- [97] Luo Z, Kim S, Kawamoto N, Rappe AM, Johnson ATC. Growth Mechanism of Hexagonal-Shape Graphene Flakes with Zigzag Edges. *ACS Nano* 2011;5:9154-60.
- [98] Treier M, Pignedoli CA, Laino T, Rieger R, Müllen K, Passerone D, Fasel R. Surface-assisted cyclodehydrogenation provides a synthetic route towards easily processable and chemically tailored nanographenes. *Nature Chem* 2011;3:61-7.
- [99] Robinson VNE, Robins JL. Nucleation kinetics of gold deposited onto UHV cleaved surfaces of NaCl and KBr. *Thin Solid Films* 1974;20:155-75.

- [100] McCarty KF, Feibelman PJ, Loginova E, Bartelt NC. Kinetics and thermodynamics of carbon segregation and graphene growth on Ru (0001). *Carbon* 2009;47:1806-13.
- [101] Nie S, Wofford JM, Bartelt NC, Dubon OD, McCarty KF. Origin of the mosaicity in graphene grown on Cu (111). *Phys Rev B* 2011;84:155425.
- [102] Avrami M. Kinetics of Phase Change. I General Theory. *J Chem Phys* 1939;7:1103-12.
- [103] Kim H, Saiz E, Chhowalla M, Mattevi C. Modeling of the self-limited growth in catalytic chemical vapor deposition of graphene. *New J Phys* 2013;15:053012.
- [104] Teng P-Y, Lu C-C, Akiyama-Hasegawa K, Lin Y-C, Yeh C-H, Suenaga K, Chiu P-W. Remote Catalyzation for Direct Formation of Graphene Layers on Oxides. *Nano Lett* 2012;12:1379-84.
- [105] Kuwana K, Li T, Saito K. Gas-phase reactions during CVD synthesis of carbon nanotubes: Insights via numerical experiments. *Chem Eng Sci* 2006;61:6718-26.
- [106] Robertson J, Zhong G, Esconjauregui S, Zhang C, Fouquet M, Hofmann S. Chemical vapor deposition of carbon nanotube forests. *Phys Status Solidi B* 2012;249:2315-22.
- [107] Youn SK, Frouzakis CE, Gopi BP, Robertson J, Teo KBK, Park HG. Temperature gradient chemical vapor deposition of vertically aligned carbon nanotubes. *Carbon* 2013;54:343-52.
- [108] Hu B, Ago H, Ito Y, Kawahara K, Tsuji M, Magome E, Sumitani K, Mizuta N, Ikeda K-i, Mizuno S. Epitaxial growth of large-area single-layer graphene over Cu(111)/sapphire by atmospheric pressure CVD. *Carbon* 2012;50:57-65.
- [109] Riikonen S, Krasheninnikov AV, Halonen L, Nieminen RM. The Role of Stable and Mobile Carbon Adspecies in Copper-Promoted Graphene Growth. *J Phys Chem C* 2012;116:5802-9.
- [110] Bhaviripudi S, Jia X, Dresselhaus MS, Kong J. Role of Kinetic Factors in Chemical Vapor Deposition Synthesis of Uniform Large Area Graphene Using Copper Catalyst. *Nano Lett* 2010;10:4128-33.
- [111] Choi J-H, Li Z, Cui P, Fan X, Zhang H, Zeng C, Zhang Z. Drastic reduction in the growth temperature of graphene on copper via enhanced London dispersion force. *Sci Rep* 2013;3.
- [112] Au C-T, Ng C-F, Liao M-S. Methane Dissociation and Syngas Formation on Ru, Os, Rh, Ir, Pd, Pt, Cu, Ag, and Au: A Theoretical Study. *J Catal* 1999;185:12-22.
- [113] Gajewski G, Pao C-W. Ab initio calculations of the reaction pathways for methane decomposition over the Cu (111) surface. *J Chem Phys* 2011;135:064707-9.
- [114] Liu L, Zhou H, Cheng R, Chen Y, Lin Y-C, Qu Y, Bai J, Ivanov IA, Liu G, Huang Y, Duan X. A systematic study of atmospheric

- pressure chemical vapor deposition growth of large-area monolayer graphene. *J Mater Chem* 2012;22:1498-503.
- [115] Mehdipour H, Ostrikov K. Kinetics of Low-Pressure, Low-Temperature Graphene Growth: Toward Single-Layer, Single-Crystalline Structure. *ACS Nano* 2012;6:10276-86.
- [116] Zhao L, Rim KT, Zhou H, He R, Heinz TF, Pinczuk A, Flynn GW, Pasupathy AN. Influence of copper crystal surface on the CVD growth of large area monolayer graphene. *Solid State Commun* 2011;151:509-13.
- [117] Wofford JM, Nie S, McCarty KF, Bartelt NC, Dubon OD. Graphene Islands on Cu Foils: The Interplay between Shape, Orientation, and Defects. *Nano Lett* 2010;10:4890-6.
- [118] Zwietering M, Jongenburger I, Rombouts F, Van't Riet K. Modeling of the bacterial growth curve. *Appl Environ Microbiol* 1990;56:1875-81.
- [119] Nie S, Wu W, Xing S, Yu Q, Pei S, McCarty KF. Growth from Below: Bilayer Graphene on Copper by Chemical Vapor Deposition. *Arxiv preprint arXiv:12021031* 2012.
- [120] Egloff G. The reactions of pure hydrocarbons: Reinhold Publishing Corporation; 1937.
- [121] Hayashi K, Sato S, Ikeda M, Kaneta C, Yokoyama N. Selective Graphene Formation on Copper Twin Crystals. *J Am Chem Soc* 2012;134:12492-8.
- [122] Yazyev OV, Pasquarello A. Effect of Metal Elements in Catalytic Growth of Carbon Nanotubes. *Physical Review Letters* 2008;100:156102.
- [123] Lizzit S, Baraldi A. High-resolution fast X-ray photoelectron spectroscopy study of ethylene interaction with Ir (0001): From chemisorption to dissociation and graphene formation. *Catal Today* 2010;154:68-74.
- [124] Plonka A. 4 Dispersive kinetics. *Annu Rep Prog Chem Sect C: Phys Chem* 2001;97:91-147.
- [125] Siebrand W, Wildman TA. Dispersive kinetics: a structural approach to nonexponential processes in disordered media. *Acc Chem Res* 1986;19:238-43.
- [126] Skrdla PJ. Roles of Nucleation, Denucleation, Coarsening, and Aggregation Kinetics in Nanoparticle Preparations and Neurological Disease. *Langmuir* 2012;28:4842-57.
- [127] Zhan L, Qiu Z, Xu Z. Separating zinc from copper and zinc mixed particles using vacuum sublimation. *Sep Purif Technol* 2009;68:397-402.
- [128] Cayré MaE, Vignolo G, Garro O. Modeling lactic acid bacteria growth in vacuum-packaged cooked meat emulsions stored at three temperatures. *Food Microbiol* 2003;20:561-6.

- [129] Zwietering M, De Koos J, Hasenack B, De Witt J, Van't Riet K. Modeling of bacterial growth as a function of temperature. *Appl Environ Microbiol* 1991;57:1094-101.
- [130] Wu P, Zhang W, Li Z, Yang J, Hou JG. Communication: Coalescence of carbon atoms on Cu (111) surface: Emergence of a stable bridging-metal structure motif. *J Chem Phys* 2010;133:071101-4.
- [131] Sinfelt JH, Carter JL, Yates DJC. Catalytic hydrogenolysis and dehydrogenation over copper-nickel alloys. *J Catal* 1972;24:283-96.
- [132] Franklin JL, Field FH. Some Aspects of the Dissociation of Benzene Under Electronic Impact. *Journal of Chemical Physics* 1953;21:2082-3.
- [133] Sinfelt JH, Yates DJC. Catalytic hydrogenolysis of ethane over the noble metals of Group VIII. *J Catal* 1967;8:82-90.
- [134] Chen Y, Vlachos DG. Hydrogenation of Ethylene and Dehydrogenation and Hydrogenolysis of Ethane on Pt(111) and Pt(211): A Density Functional Theory Study. *J Phys Chem C* 2010;114:4973-82.
- [135] Saucedo-Castañeda G, Raimbault M, Viniestra-González G. Energy of activation in cassava silages. *J Sci Food Agric* 1990;53:559-62.
- [136] Vlassioug I, Regmi M, Fulvio P, Dai S, Datskos P, Eres G, Smirnov S. Role of Hydrogen in Chemical Vapor Deposition Growth of Large Single-Crystal Graphene. *ACS Nano* 2011;5:6069-76.
- [137] Choubak S, Biron M, Levesque PL, Martel R, Desjardins P. No Graphene Etching in Purified Hydrogen. *J Phys Chem Lett* 2013;4:1100-3.
- [138] Jacobberger RM, Arnold MS. Graphene Growth Dynamics on Epitaxial Copper Thin Films. *Chem Mater* 2013;25:871-7.
- [139] Yu Q, Jauregui LA, Wu W, Colby R, Tian J, Su Z, Cao H, Liu Z, Pandey D, Wei D. Control and characterization of individual grains and grain boundaries in graphene grown by chemical vapour deposition. *Nature Materials* 2011;10:443-9.
- [140] Robertson AW, Warner JH. Hexagonal Single Crystal Domains of Few-Layer Graphene on Copper Foils. *Nano Lett* 2011;11:1182-9.
- [141] Nie S, Walter AL, Bartelt NC, Starodub E, Bostwick A, Rotenberg E, McCarty KF. Growth from Below: Graphene Bilayers on Ir(111). *ACS Nano* 2011;5:2298-306.
- [142] Nie S, Wu W, Xing S, Yu Q, Bao J, Pei S-s, McCarty KF. Growth from below: bilayer graphene on copper by chemical vapor deposition. *New J Phys* 2012;14:093028.
- [143] Han Z, Kimouche A, Allain A, Arjmandi-Tash H, Reserbat-Plantey A, Pairis S, Reita V, Bendiab N, Coraux J, Bouchiat V. Suppression of Multilayer Graphene Patches during CVD Graphene growth on Copper. *arXiv preprint arXiv:12051337* 2012.

- [144] Wassei JK, Mecklenburg M, Torres JA, Fowler JD, Regan BC, Kaner RB, Weiller BH. Chemical Vapor Deposition of Graphene on Copper from Methane, Ethane and Propane: Evidence for Bilayer Selectivity. *Small* 2012;8:1415-22.
- [145] Dai B, Fu L, Zou Z, Wang M, Xu H, Wang S, Liu Z. Rational design of a binary metal alloy for chemical vapour deposition growth of uniform single-layer graphene. *Nat Comm* 2011;2:522.
- [146] Fan L, Li Z, Xu Z, Wang K, Wei J, Li X, Zou J, Wu D, Zhu H. Step driven competitive epitaxial and self-limited growth of graphene on copper surface. *AIP Adv* 2011;1:032145.
- [147] Reina A, Thiele S, Jia X, Bhaviripudi S, Dresselhaus M, Schaefer J, Kong J. Growth of large-area single- and Bi-layer graphene by controlled carbon precipitation on polycrystalline Ni surfaces. *Nano Res* 2009;2:509-16.
- [148] Huang PY, Ruiz-Vargas CS, van der Zande AM, Whitney WS, Levendorf MP, Kevek JW, Garg S, Alden JS, Hustedt CJ, Zhu Y. Grains and grain boundaries in single-layer graphene atomic patchwork quilts. *Nature* 2011;469:389-92.
- [149] Lee Y, Bae S, Jang H, Jang S, Zhu S-E, Sim SH, Song YI, Hong BH, Ahn J-H. Wafer-Scale Synthesis and Transfer of Graphene Films. *Nano Lett* 2010;10:490-3.
- [150] Srivastava A, Galande C, Ci L, Song L, Rai C, Jariwala D, Kelly KF, Ajayan PM. Novel Liquid Precursor-Based Facile Synthesis of Large-Area Continuous, Single, and Few-Layer Graphene Films. *Chem Mater* 2010;22:3457-61.
- [151] Suk JW, Kitt A, Magnuson CW, Hao Y, Ahmed S, An J, Swan AK, Goldberg BB, Ruoff RS. Transfer of CVD-grown monolayer graphene onto arbitrary substrates. *ACS Nano* 2011;5:6916-24.
- [152] Stoberl U, Wurstbauer U, Wegscheider W, Weiss D, Eroms J. Morphology and flexibility of graphene and few-layer graphene on various substrates. *Appl Phys Lett* 2008;93:051906--3.
- [153] Chen Z, Ren W, Gao L, Liu B, Pei S, Cheng H-M. Three-dimensional flexible and conductive interconnected graphene networks grown by chemical vapour deposition. *Nature Materials* 2011;10:424-8.
- [154] Jiao L, Zhang L, Wang X, Diankov G, Dai H. Narrow graphene nanoribbons from carbon nanotubes. *Nature* 2009;458:877-80.
- [155] Lin Y-C, Lu C-C, Yeh C-H, Jin C, Suenaga K, Chiu P-W. Graphene Annealing: How Clean Can It Be? *Nano Lett* 2011;12:414-9.
- [156] Chen X-D, Liu Z-B, Zheng C-Y, Xing F, Yan X-Q, Chen Y, Tian J-G. High-quality and efficient transfer of large-area graphene films onto different substrates. *Carbon* 2013;56:271-8.
- [157] Choi J-Y. Graphene transfer: A stamp for all substrates. *Nat Nano* 2013;8:311-2.

- [158] Song J, Kam F-Y, Png R-Q, Seah W-L, Zhuo J-M, Lim G-K, Ho PK, Chua L-L. A general method for transferring graphene onto soft surfaces. *Nat Nanotechnol* 2013;8:356-62.
- [159] Regan W, Alem N, Alemán B, Geng B, Girit C, Maserati L, Wang F, Crommie M, Zettl A. A direct transfer of layer-area graphene. *Appl Phys Lett* 2010;96:113102--3.
- [160] Yoon T, Shin WC, Kim TY, Mun JH, Kim T-S, Cho BJ. Direct Measurement of Adhesion Energy of Monolayer Graphene As-Grown on Copper and Its Application to Renewable Transfer Process. *Nano Lett* 2012;12:1448-52.
- [161] Wang Y, Zheng Y, Xu X, Dubuisson E, Bao Q, Lu J, Loh KP. Electrochemical Delamination of CVD-Grown Graphene Film: Toward the Recyclable Use of Copper Catalyst. *ACS Nano* 2011;5:9927-33.
- [162] Gao L, Ren W, Xu H, Jin L, Wang Z, Ma T, Ma L-P, Zhang Z, Fu Q, Peng L-M. Repeated growth and bubbling transfer of graphene with millimetre-size single-crystal grains using platinum. *Nat Comm* 2012;3:699.
- [163] Pirkle A, Chan J, Venugopal A, Hinojos D, Magnuson C, McDonnell S, Colombo L, Vogel E, Ruoff R, Wallace R. The effect of chemical residues on the physical and electrical properties of chemical vapor deposited graphene transferred to SiO<sub>2</sub>. *Appl Phys Lett* 2011;99:122108--3.
- [164] Liang X, Sperling BA, Calizo I, Cheng G, Hacker CA, Zhang Q, Obeng Y, Yan K, Peng H, Li Q, Zhu X, Yuan H, Hight Walker AR, Liu Z, Peng L-m, Richter CA. Toward Clean and Crackless Transfer of Graphene. *ACS Nano* 2011;5:9144-53.
- [165] O'Hern SC, Stewart CA, Boutilier MS, Idrobo J-C, Bhaviripudi S, Das SK, Kong J, Laoui T, Atieh M, Karnik R. Selective molecular transport through intrinsic defects in a single layer of CVD graphene. *ACS Nano* 2012;6:10130-8.
- [166] Gonçalves G, Marques PA, Barros-Timmons A, Bdkin I, Singh MK, Emami N, Grácio J. Graphene oxide modified with PMMA via ATRP as a reinforcement filler. *J Mater Chem* 2010;20:9927-34.
- [167] Ishigami M, Chen JH, Cullen WG, Fuhrer MS, Williams ED. Atomic Structure of Graphene on SiO<sub>2</sub>. *Nano Lett* 2007;7:1643-8.
- [168] Ou E, Xie Y, Peng C, Song Y, Peng H, Xiong Y, Xu W. High concentration and stable few-layer graphene dispersions prepared by the exfoliation of graphite in different organic solvents. *RSC Adv* 2013;3:9490-9.
- [169] Hernandez Y, Nicolosi V, Lotya M, Blighe FM, Sun Z, De S, McGovern I, Holland B, Byrne M, Gun'Ko YK. High-yield production of graphene by liquid-phase exfoliation of graphite. *Nat Nanotechnol* 2008;3:563-8.

- [170] Du W, Lu J, Sun P, Zhu Y, Jiang X. Organic salt-assisted liquid-phase exfoliation of graphite to produce high-quality graphene. *Chem Phys Lett* 2013;568–569:198-201.
- [171] Hesjedal T. Continuous roll-to-roll growth of graphene films by chemical vapor deposition. *Appl Phys Lett* 2011;98:133106-3.
- [172] Yamada T, Ishihara M, Kim J, Hasegawa M, Iijima S. A roll-to-roll microwave plasma chemical vapor deposition process for the production of 294&#xa0;mm width graphene films at low temperature. *Carbon* 2012;50:2615-9.
- [173] Su C-Y, Lu A-Y, Wu C-Y, Li Y-T, Liu K-K, Zhang W, Lin S-Y, Juang Z-Y, Zhong Y-L, Chen F-R, Li L-J. Direct Formation of Wafer Scale Graphene Thin Layers on Insulating Substrates by Chemical Vapor Deposition. *Nano Lett* 2011;11:3612-6.
- [174] Peng Z, Yan Z, Sun Z, Tour JM. Direct Growth of Bilayer Graphene on SiO<sub>2</sub> Substrates by Carbon Diffusion through Nickel. *ACS Nano* 2011;5:8241-7.
- [175] Bi H, Sun S, Huang F, Xie X, Jiang M. Direct growth of few-layer graphene films on SiO<sub>2</sub> substrates and their photovoltaic applications. *J Mater Chem* 2012;22:411-6.
- [176] Fanton MA, Robinson JA, Puls C, Liu Y, Hollander MJ, Weiland BE, LaBella M, Trumbull K, Kasarda R, Howsare C, Stitt J, Snyder DW. Characterization of Graphene Films and Transistors Grown on Sapphire by Metal-Free Chemical Vapor Deposition. *ACS Nano* 2011;5:8062-9.
- [177] Hwang J, Shields VB, Thomas CI, Shivaraman S, Hao D, Kim M, Woll AR, Tompa GS, Spencer MG. Epitaxial growth of graphitic carbon on C-face SiC and sapphire by chemical vapor deposition (CVD). *J Cryst Growth* 2010;312:3219-24.
- [178] Miyasaka Y, Nakamura A, Temmyo J. Graphite Thin Films Consisting of Nanograins of Multilayer Graphene on Sapphire Substrates Directly Grown by Alcohol Chemical Vapor Deposition. *Jpn J Appl Phys* 2011;50:04DH12.
- [179] Liu Z, Song L, Zhao S, Huang J, Ma L, Zhang J, Lou J, Ajayan PM. Direct Growth of Graphene/Hexagonal Boron Nitride Stacked Layers. *Nano Lett* 2011;11:2032-7.
- [180] Lippert G, Dabrowski J, Lemme M, Marcus C, Seifarth O, Lupina G. Direct graphene growth on insulator. *Phys Status Solidi B* 2011;248:2619-22.
- [181] Rummeli MH, Bachmatiuk A, Scott A, Borner F, Warner JH, Hoffman V, Lin J-H, Cuniberti G, Buchner B. Direct low-temperature nanographene CVD synthesis over a dielectric insulator. *ACS Nano* 2010;4:4206-10.





## Curriculum Vitae

Name: Kemal Celebi  
Date of Birth: February 13<sup>th</sup>, 1982  
Place of Birth: Isparta, Turkey  
Nationality: Turkish

- 09/09-09/13 PhD Candidate in Engineering  
Nanoscience for Energy Technology & Sustainability, Institute of Energy Technology, Department of Mechanical and Process Engineering, ETH Zurich, Switzerland  
Supervisor: Prof. Hyung Gyu Park
- 09/04-01/08 Master's Thesis in Physics  
Soft Semiconductor Group, Research Laboratory of Electronics, Massachusetts Institute of Technology, United States of America  
Supervisor: Prof. Marc A. Baldo
- 09/00-06/04 Undergraduate Study in Physics  
Bilkent University, Turkey

## List of Publications

### Peer-reviewed Journal Publications (during PhD study)

1. K. Celebi, M. T. Cole, K. Teo and H. G. Park. Chemical Vapor Deposition of Graphene on Copper, **CRC Handbook of Graphene Science**, Vol 4: Mechanical and Chemical Properties. *Book chapter, submitted*.
2. K. Celebi, M. T. Cole, J. W. Choi, N. Rupeshinge, F. Wyczisk, P. Legagneux, J. Robertson, K. B. K. Teo and H. G. Park. Evolutionary Kinetics of Chemical Vapor Deposition of Graphene on Copper, **Nano Letters** 13, (2013).
3. K. Celebi, M. T. Cole, N. Rupesinghe, P. Greenwood, L. Tao, D. Akinwande, J. Robertson, H. G. Park and K. B. K. Teo. Growth Kinetics and Uniform Scaling-up of Graphene Synthesis, **ECS Transactions** 53, (2013).
4. K. Celebi, M. T. Cole, K. B. K. Teo and H. G. Park. Observations of Early Stage Graphene Growth on Copper, **Electrochemical and Solid State Letters** 15, (2012).
5. K. Celebi, A. O. Altun, K. B. K. Teo and H. G. Park. Observation of the Graphene Surface Structure at the Early Stages of Graphene Growth on Copper, **ECS Transactions** 35, (2011).

### Peer-reviewed Journal Publications (past)

6. M. Fischer, G. Scalari, K. Celebi, M. Amanti, C. Walther, M. Beck and J. Faist. Scattering Processes in terahertz InGaAs/InAlAs quantum Cascade Lasers, **Applied Physics Letters** 97, 221114 (2010).
7. M. Bora, K. Celebi, C. Zuniga, C. P. Watson, K. Milaninia and M.A. Baldo. Near field detector for integrated surface plasmon resonance biosensor applications, **Optics Express** 17, 329-336 (2009).
8. K. Celebi, P. Jadhav, K. Milaninia, M. Bora and M.A. Baldo. The Density Of States In Thin Film Copper Phthalocyanine Measured By Kelvin Probe Force

- Microscopy, **Applied Physics Letters** 93, 083308 (2008).
9. J.K. Mapel, K. Celebi, M. Singh, and M.A. Baldo. Plasmonic Excitation of Organic Double Heterostructure Solar Cells. **Applied Physics Letters** 90, 121102 (2007).
  10. T.D. Heidel, J.K. Mapel, M. Singh, K. Celebi, and M.A. Baldo. Surface Plasmon Polariton Mediated Energy Transfer in Organic Photovoltaic Devices. **Applied Physics Letters** 91, 093506 (2007).
  11. C.L. Mulder, K. Celebi, K. M. Milaninia and M.A. Baldo. Saturated and Efficient Blue Phosphorescent Organic Light Emitting Devices with Lambertian Angular Emission, **Applied Physics Letters** 90, 211109 (2007).
  12. K. Celebi, T.D. Heidel and M.A. Baldo. Simplified Calculation of Dipole Energy Transport in a Multilayer Stack Using Dyadic Green's Functions, **Optics Express** 15, 1762-1772 (2007).
  13. Near field detector for integrated surface plasmon resonance biosensor applications, M. A. Baldo, M. Bora, K. Celebi, J. K. Mapel. Patent application. (2008) *PCT/US2008/084843*.
  14. Organic Light Emitting Device, M.A. Baldo, K. Celebi, C. L. Mulder. Patent application. (2008) *US2008/0309217 A1*.

#### Conference Talks (during PhD study)

1. K. Celebi, M. T. Cole, J. W. Choi, J. Robertson, K. B. K. Teo and H. G. Park. '*Kinetics of graphene synthesis on copper*', **MRS Spring Meeting 2013**, San Francisco, U.S.A.
2. K. Celebi, M. Cole, J. W. Choi, K. B. K. Teo and H. G. Park. '*Kinetics of chemical vapor deposition of graphene on copper*', **Nanotech 2012**, Santa Clara, U.S.A. (invited talk)
3. K. Celebi, J. W. Choi, M. Cole, K. B. K. Teo and H. G. Park. '*Early stages of graphene growth on copper*', **e-MRS Spring Meeting 2012**, Strasbourg, France. (invited talk)

4. K. Celebi, D. Engstrom, N. Y. Wu, C. König, N. Rupesinghe, K. B. K. Teo and H. G. Park. *Investigation of hydrogen annealing and rapid cooling on the epitaxial growth of graphene on silicon carbide*, **MRS Spring Meeting 2010**, San Francisco, U.S.A.